UNIVERSIDADE FEDERAL DO RIO GRANDE DO SUL
INSTITUTO DE FÍSICA
PROGRAMA DE PÓS-GRADUAÇÃO EM FÍSICA

Principles of Tissue Self-Organization: Differential Contractility and Collective Aggregation

Emanuel F. Teixeira

PhD Thesis presented to the Graduate Program in Physics at Universidade Federal do Rio Grande do Sul to obtain the PhD title in Physics.

Supervisor: Prof. Leonardo Gregory Brunnet
Co-supervisor: Prof. Heitor Marques Fernandes
Research field: Active Matter, Biological Physics
Concentration area: Statistical Physics

Porto Alegre - RS
2025

Acknowledgments

I would like to express my deepest gratitude to my supervisor, Prof. Leonardo Gregory Brunnet, for his invaluable guidance, encouragement, and continuous support throughout this thesis. I am also sincerely grateful to my co-supervisor, Prof. Heitor Marques Fernandes, for his insights, patience, and constructive advice.

My deepest thanks go to my parents, Sandra and Sérgio, whose unwavering dedication and sacrifices made it possible for me to pursue higher education and to reach this stage of my academic journey. I am grateful to my sister, Vitória, for her constant support and affection whenever I needed it.

A very special acknowledgment is due to my late brother, Alan, whose inspiring conversations about the vastness of the cosmos and the beauty of the universe encouraged me to follow my dream of becoming an academic in Physics. I also thank my niece, Manuella, who, during the quarantine, often came to my room to watch the computer simulations that sparked her curiosity.

To my partner, Nathália, I owe heartfelt gratitude for her love, patience, and encouragement throughout my doctoral studies, my master's, and even part of my undergraduate years.

Finally, I warmly thank my colleagues and friends for their support and companionship during this PhD. Among my colleagues, I am deeply grateful to Pablo, Davi, Paulo, and Carine. The excellent academic discussions we shared were fundamental to the development of this work.

I would like to thank all the institutions that have financially supported me: the Coordenação de Aperfeiçoamento de Pessoal de Nível Superior (CAPES), for my PhD scholarship, and the Fundação de Amparo à Pesquisa do Estado de São Paulo (FAPESP), for the invaluable support of my participation in events at the ICTP-SAIFR, a fundamental experience for my personal growth and for building important scientific collaborations. I would like to thank the institutions where I could develop this work, first my home university Universidade Federal do Rio Grande do Sul (UFRGS), and I am also grateful to the Universidade Estadual Paulista (UNESP), for the warm hospitality during my many visits.

"If I have seen further it is by standing on the shoulders of giants."
— Isaac Newton

Resumo

A auto-organização de células individuais em tecidos funcionais é um exemplo paradigmático de emergência de ordem em biologia. Compreender os princípios físicos que governam este processo é um desafio central na física biologica e na biologia do desenvolvimento. Esta tese aborda este desafio sob a ótica da matéria ativa, investigando dois mecanismos essenciais e sequenciais na construção de tecidos: a segregação celular e a cinética de agregação.

Na primeira parte, investigamos a Hipótese da Contração Diferencial de Superfície (DSCH), que postula que diferenças na contratilidade cortical ativa, em vez da adesão, podem impulsionar a segregação. Para testar essa hipótese de forma isolada, desenvolvemos um modelo computacional inédito de membranas ativas deformáveis. Nossos resultados demonstram que a contratilidade diferencial é, por si só, suficiente para promover a segregação, validando a DSCH como um mecanismo robusto para a formação de padrões teciduais. A análise cinética revelou que o crescimento dos domínios ocorre por meio da coalescência de agregados.

Na segunda parte, abordamos a questão das cinéticas de agregação anômalas observadas em sistemas celulares, que frequentemente ocorrem em velocidades muito superiores às previstas por teorias clássicas. Utilizando a equação de coagulação de Smoluchowski e simulações de partículas autopropelidas com um mecanismo de autoalinhamento, demonstramos que uma transição para o movimento coletivo (flocking) dentro dos agregados dá origem a um novo regime que denominamos agregação balística coletiva. Este mecanismo explica a emergência de expoentes de crescimento anômalos e fornece um arcabouço unificado que reconcilia uma vasta gama de observações experimentais e numéricas.

Por fim, esta tese aprofunda a compreensão física da formação de tecidos, conectando as interações em nível celular com a organização macroscópica. O trabalho valida um mecanismo fundamental de segregação e resolve um quebra-cabeça de longa data sobre a velocidade da agregação, oferecendo um framework unificado para interpretar a dinâmica de auto-organização em matéria ativa.

Palavras-chave: Matéria Ativa, Segregação Celular, Contratilidade Celular, Movimento Coletivo, Agregação Balística Coletiva.

Abstract

The self-organization of individual cells into functional tissues is a paradigmatic example of emergent order in biology. Understanding the physical principles governing this process is a central challenge in biological physics and developmental biology. This thesis addresses this challenge from the perspective of active matter, investigating two essential and sequential mechanisms in tissue construction: cell segregation and aggregation kinetics.

In the first part, we investigate the Differential Surface Contraction Hypothesis (DSCH), which posits that differences in active cell contractility, rather than adhesion, can drive segregation. To test this hypothesis in isolation, we developed a novel computational model of deformable active membranes. Our results demonstrate that differences in contractility are, by themselves, sufficient to drive cell segregation, thereby validating the DSCH as a robust mechanism for tissue patterning.

In the second part, we address the issue of anomalous aggregation kinetics observed in cellular systems, which are often much faster than the predictions of classical theories. Using Smoluchowski's coagulation theory and simulations of self-propelled particles with a self-alignment mechanism, we show that a transition to collective motion (flocking) at the cluster level gives rise to a new regime we term collective ballistic aggregation. This mechanism explains the emergence of accelerated growth exponents and unifies diverse experimental and numerical observations.

Taken together, this thesis offers an in depth mechanistic understanding of tissue formation, connecting interactions at the cell level with macroscopic organization. The work provides a unified theoretical framework for interpreting the mechanisms of segregation and the scaling laws of aggregation in active matter systems, both biological and synthetic.

Keywords: Active Matter, Cell Segregation, Cellular Contractility, Collective Motion, Collective Ballistic Aggregation.

Contents

Introduction

The formation of functional tissues and organs from initially disordered cell populations is one of the most remarkable examples of self-organization in biology [1–7]. This process, fundamental to morphogenesis and embryonic development, depends on a complex dynamics of cellular interactions. A central challenge in developmental and biological physics is to decipher the physical principles governing how local, microscopic interactions among individual cells give rise to robust and functional organization at the macroscopic tissue scale.

Importantly, biological cells behave as active systems [8–11]: they continuously consume energy to generate mechanical forces and motion, operating far from thermodynamic equilibrium [9]. This active nature distinguishes living tissues from passive materials, as cells can actively migrate [12], change shape [13] and exert active contractile forces [14–18]. Moreover, through an internal feedback mechanism, individual cells can exhibit self-alignment, continuously adjusting their polarity (self-propulsion direction) to match their own velocity, which arises from the interplay between self-propulsion and mechanical interactions with neighboring cells [19, 20]. Consequently, tissues exhibit emergent collective dynamics that cannot be explained solely by equilibrium physics or passive adhesion models. Recognizing cells as active matter units is essential for understanding mechanisms such as cell segregation and collective cell aggregation which are fundamental in tissue formation.

This thesis addresses this challenge by investigating two sequential and essential mechanisms in tissue construction: **cell segregation (sorting)** and **collective cell aggregation**. Cell segregation is the ability of heterogeneous cell types to separate and organize into homogeneous groups, a central process for establishing distinct tissue layers and organs during development [1–7]. Collective aggregation concerns the dynamic formation and growth of cellular clusters that determine the macroscopic properties, morphology, and functionality of tissues.

Several hypotheses have been proposed to explain cell segregation, including the Differential Adhesion Hypothesis (DAH) [1], which attributes segregation to differences in adhesion strength between cell types; the Differential Surface Contraction Hypothesis (DSCH) [14], which emphasizes differences in cell's contractility; and the Differential Interfacial Tension Hypothesis (DITH) [21], which considers effective tensions at cell–cell interfaces. While DAH has been extensively studied, the DSCH remains less explored and is the main focus of the first part of this thesis.

Beyond which mechanisms drive segregation, an equally fundamental question is how and at what rate this process of domain formation occurs. Classical cluster growth processes, such as Ostwald ripening [22–24], diffusion-limited cluster aggregation (DLCA) [25–28], and ballistic aggregation [25, 29], predict algebraic growth laws with exponents that are smaller than those observed in certain biological systems. Experiments with cell cultures have revealed anomalously fast aggregation kinetics, with growth exponents that

defy conventional theoretical explanations [5]. The physical origin of this accelerated behavior, driven by the collective active motion of cells [30, 31], is not yet fully elucidated.

This problems is addressed through two complementary lines of research:

- **Contractility-driven segregation in deformable active membranes** — The first part focuses on the DSCH, which proposes that differences in contractility can drive cell segregation in tissues, independently of adhesion differences. To test this hypothesis, we develop a model of deformable active membranes, in which each cell is represented as an elastic, self-propelled closed contour with tunable stiffness and contractility. This approach allows us to isolate the role of contractility, reveal conditions under which segregation occurs, and quantify its kinetics. The model also provides a versatile platform for exploring the interplay between mechanical parameters and emergent patterns.

- **Aggregation kinetics in active systems** — The second part of this thesis addresses the kinetics of cluster growth, motivated by the observation that cellular systems often aggregate much faster than predicted by classical theories. Focusing on the internal cells (endoderm) from a kinetic theory perspective, we investigate how internal alignment within clusters can induce a transition to highly persistent, collective motion. Using analytical approaches based on Smoluchowski's coagulation equation, complemented by simulations of adhesive active particles with self-alignment, we show that this collective behavior gives rise to a novel collective ballistic aggregation regime, providing a unified framework that explains the wide spectrum of aggregation rates observed in active matter.

The thesis is structured as follows. Part I introduces the main hypotheses of cell segregation (DAH, DSCH, and DITH) and the computational models commonly used to test them. It then presents the deformable active membrane model, its validation, and its application to the DSCH. Part II turns to kinetic theory, deriving analytical predictions for ballistic aggregation and comparing them with simulation results. Finally, the Conclusions summarize the main findings, discuss their implications, and outline perspectives for future work.

Part I

Mechanisms of Cell Segregation

Chapter 1

Mechanical Hypotheses of Cell Segregation

Cell segregation is a paradigmatic case of biological self-organization, where initially disordered populations of cells spontaneously rearrange into structured and functionally coherent tissues [1, 4–6, 18]. This emergent collective behavior underlies key developmental processes, including tissue stratification, compartment boundary formation, and organogenesis [32]. A central challenge in this context is to identify the physical principles that govern how local interactions among cells give rise to robust macroscopic organization at the tissue level.

One of the most compelling demonstrations of this self-organizing capacity comes from experiments in which embryonic tissues are dissociated and their constituent cells are randomly reaggregated. Notably, cells originating from different histological types are able to autonomously sort and reconstitute morphologically accurate structures. This process, suggests that segregation is driven by intrinsic physical mechanisms that do not depend on external patterning cues [33–37].

Over the past decades, several theoretical frameworks have been proposed to explain the driving forces behind cell segregation. These hypotheses differ in how they balance passive adhesive forces and active contractile behaviors, leading to distinct mechanistic interpretations. While some models emphasize differences in cell–cell adhesion (e.g., the Differential Adhesion Hypothesis, DAH) [1], others argue that active processes such as cortical tension are essential (e.g., the Differential Surface Contraction Hypothesis, DSCH) [14], or propose integrative approaches combining both effects (e.g., the Differential Interfacial Tension Hypothesis, DITH) [21].

In this chapter, we present a systematic overview of the main mechanical hypotheses proposed to explain cell segregation. We begin with the foundational Differential Adhesion Hypothesis (DAH), which describes segregation as a passive process driven by differences in adhesion. We then examine the Differential Interfacial Tension Hypothesis (DITH), which extends the DAH by incorporating active contraction tension into the mechanical balance at cell–cell interfaces. Finally, we turn to the Differential Surface Contraction Hypothesis (DSCH), which proposes that differences in active surface contractility alone may be sufficient to drive segregation, even in the absence of adhesion. Throughout the chapter, we critically discuss the assumptions, predictions, and limitations of each framework. We conclude by motivating the development of a new computational model designed to isolate and test the DSCH as a standalone mechanism, allowing us to directly evaluate whether differential active tension alone can account for robust cell segregation.

1.1 The Differential Adhesion Hypothesis (DAH)

The first comprehensive physical framework to explain cell segregation was the *Differential Adhesion Hypothesis* (DAH), proposed by Malcolm Steinberg in the 1960s [1]. Using an analogy with the behavior of immiscible liquids, the DAH states that the spatial organization of cells within a tissue arises from differences in intercellular adhesion. According to this view, cells rearrange to minimize the system's total adhesive energy, much like fluid droplets minimize their surface free energy by reducing high-tension interfaces. As a result, cells that adhere more strongly to each other tend to cluster together, leading to a thermodynamically stable configuration governed by adhesive preferences.

Steinberg argued that the driving force for segregation lies in the differential energy required to maintain homotypic (between cells of the same type) and heterotypic (different type) contacts. The system's total adhesive energy is minimized when cells preferentially form energetically favorable homotypic interactions while reducing costly heterotypic interfaces. This principle allows the DAH to make predictions about the final configuration of mixed cell populations, based on the relative strengths of adhesion between different cell types. These adhesive interactions are denoted as:

- A_{11}: homotypic adhesion between cells of type 1,
- A_{22}: homotypic adhesion between cells of type 2,
- $A_{12} = A_{21}$: heterotypic adhesion between cells of types 1 and 2.

Based on these parameters, the DAH predicts three outcomes [1]:

1. **Segregation:** If heterotypic adhesion is smaller than homotypic adhesion, the two cell populations will segregate into distinct domains (Fig. 1.1a), which is described by the relation $A_{12} < \frac{A_{11}+A_{22}}{2}$.
2. **Engulfment of type 1 by type 2:** If heterotypic adhesion is weaker than homotypic adhesion, and the homotypic adhesion among type 2 cells is equal to or weaker than the heterotypic one, then the system undergoes segregation, and type 1 cells become engulfed by type 2 cells (Fig. 1.1b). This configuration is defined by the condition: $A_{22} \leq A_{12} < \frac{A_{11}+A_{22}}{2}$.
3. **Checkerboard pattern:** If $A_{12} > \frac{A_{11}+A_{22}}{2}$, heterotypic adhesion is favorable, resulting in an intermixed configuration with alternating cell types (Fig. 1.1c).

To formalize Steinberg's hypothesis quantitatively, Graner et al. [39, 40] introduced in 1993 a surface energy–based framework that reformulated the DAH in terms of surface contact energies. In this approach, a tissue is modeled as a mixture of cells embedded in a surrounding medium, and the total surface energy of the system is defined as:

$$E = \sum_{(i,j)} a_{ij}\, e_{ij} + \sum_{i} a_{iM}\, e_{iM}, \tag{1.1}$$

where a_{ij} denotes the contact area between cells of types i and j, and a_{iM} represents the contact area between cell i and the surrounding medium. The terms $e_{ij} = e_{ji}$ and e_{iM} correspond to the respective surface energy densities associated with cell–cell and cell–medium interactions.

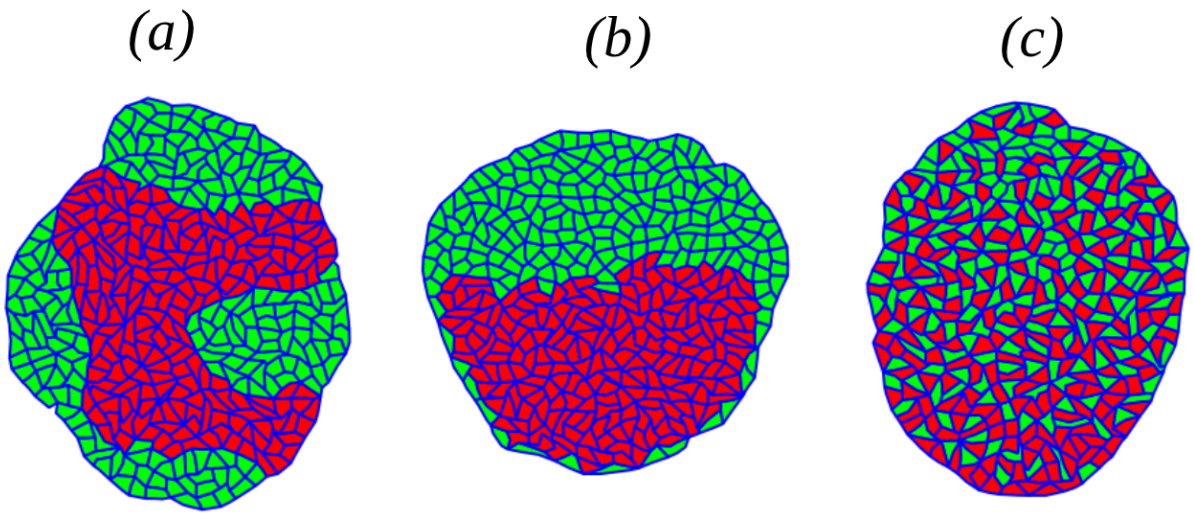

Figure 1.1: Figure adapted from Wolff et al. [38]. Illustrative outcomes predicted by the Differential Adhesion Hypothesis (DAH) for two interacting cell types, based on their homotypic and heterotypic adhesion energies. (a) **Segregation:** When heterotypic adhesion is weaker than the average homotypic adhesion ($A_{12} < \frac{A_{11}+A_{22}}{2}$), cells minimize contact energy by segregation into distinct, homogenous domains. (b) **Engulfment:** A particular case of segregation in which type 2 cells fully surround and engulf type 1 cells. This occurs when heterotypic adhesion is weaker than the average homotypic adhesion, and type 2 cohesion is not stronger than heterotypic adhesion ($A_{22} \leq A_{12} < \frac{A_{11}+A_{22}}{2}$). (c) **Checkerboard pattern:** When heterotypic adhesion is stronger than or equal to the average homotypic adhesion ($A_{12} > \frac{A_{11}+A_{22}}{2}$), cells preferentially form heterotypic contacts, resulting in an intermixed, alternating configuration.

Graner's formulation not only recovers the qualitative predictions of Steinberg but also enables more precise modeling of multicellular configurations. Based on energetic minimization, three scenarios emerge depending on the relative magnitudes of surface energy densities:

- **Segregation:** Heterotypic contacts are more energetically costly than homotypic ones, i.e., $e_{12} > e_{11}$ and $e_{12} > e_{22}$, which implies:

$$e_{12} > \frac{e_{11} + e_{22}}{2} \quad \text{(Segregation)}. \tag{1.2}$$

- **Engulfment of type 1 by type 2:** This occurs when type 1 cells prefer contacting type 2 cells over the medium ($e_{12} < e_{1M}$), and type 2 cells prefer homotypic contact over the medium ($e_{22} < e_{2M}$), leading to:

$$e_{12} < e_{22} + (e_{1M} - e_{2M}) \quad \text{(Engulfment of 1 by 2)}. \tag{1.3}$$

- **Checkerboard pattern:** When heterotypic adhesion is energetically favorable compared to both homotypic adhesions, i.e., $e_{12} < e_{11}$ and $e_{12} < e_{22}$, the condition becomes:

$$e_{12} < \frac{e_{11} + e_{22}}{2} \quad \text{(Checkerboard)}. \tag{1.4}$$

1.1.1 The Cellular Potts Model (CPM)

To test and simulate the predictions of the Differential Adhesion Hypothesis (DAH), Graner and Glazier [41, 42] developed in the early 1990s the *Cellular Potts Model* (CPM), also known as the Glazier–Graner–Hogeweg (GGH) model. This was the first computational framework to reproduce cell segregation behaviors based on differential adhesion, effectively validating the qualitative hypothesis of Steinberg and the quantitative energy-based formulation proposed by Graner et al. [39, 40]. Through this model, they demonstrated that differential surface energies alone were sufficient to drive spontaneous cell segregation, engulfment, or intermixing, depending on the relative strengths of homotypic and heterotypic energies.

In the CPM, space is discretized into a regular lattice, typically square or hexagonal, where each lattice site carries a spin value σ indicating its association to a specific cell or to the extracellular medium. A single cell is represented as a connected cluster of lattice sites sharing the same spin. The system evolves via a stochastic Monte Carlo algorithm that mimics membrane fluctuations and cell motility: at each step, a lattice site is randomly chosen, and an attempt is made to copy the spin of a neighboring site into it. The acceptance of this move depends on the resulting change in a global energy function (Hamiltonian) $\mathcal{H}$, according to the Metropolis–Hastings criterion:

$$P(\text{accept}) = \begin{cases} 1, & \Delta\mathcal{H} \leq 0 \\ \exp(-\Delta\mathcal{H}/T), & \Delta\mathcal{H} > 0 \end{cases}$$

where T is an effective temperature that controls the amplitude of stochastic fluctuations. The Hamiltonian, $\mathcal{H}$, encodes mechanical and surface properties of the system. A commonly adopted form is:

$$\mathcal{H} = \sum_{i=1}^{N_{\text{cells}}} \left[\frac{K_A}{2} (A_i - A_0)^2 + \frac{K_P}{2} (P_i - P_0)^2 \right] + \sum_{\langle i,j \rangle} J_{\tau_i,\tau_j} (1 - \delta_{\sigma(i),\sigma(j)}), \tag{1.5}$$

where:

- A_i and P_i denote the area and perimeter of cell i, with A_0 and P_0 their respective target values;
- K_A and K_P are elastic moduli that penalize deviations from preferred size and shape;
- J_{τ_i,τ_j} represents the surface energy between types τ_i and τ_j;
- The Kronecker delta $\delta_{\sigma(i),\sigma(j)}$ ensures that only interfaces between different domains contribute to surface energy.

The first two terms model mechanical stability of individual cells, while the third term governs adhesive interactions between cells and with the medium. By tuning the surface energy parameters J_{τ_i,τ_j}, the CPM provides a direct computational means to test the energetic conditions predicted by the DAH. For instance, Graner and Glazier showed that spontaneous cell segregation occurs when heterotypic surface energy exceeds homotypic energy (see Fig. 1.2), confirming the criterion:

$$J_{12} > \frac{J_{11} + J_{22}}{2} \quad \text{(segregation)}. \tag{1.6}$$

Moreover, the model captures more complex behaviors such as the engulfment of one cell type by another, depending on relative cell–medium affinities (see Fig. 1.2). For example, aggregation and full engulfment of type 1 by type 2 is observed when:

$$J_{12} < J_{22} + (J_{1M} - J_{2M}) \quad \text{(engulfment of 1 by 2)}. \tag{1.7}$$

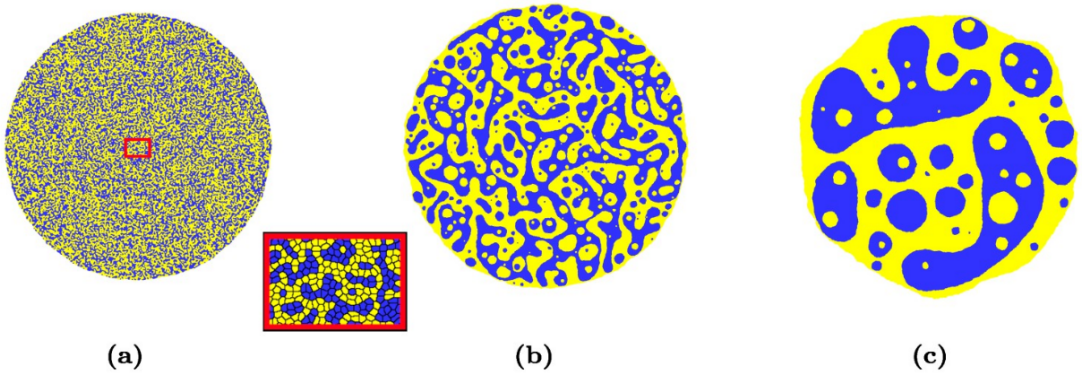

Figure 1.2: Figure reproduced from Durand et al. [43]. Time evolution of cell segregation in a Cellular Potts Model (CPM) simulation driven by differential adhesion. Starting from a random 50:50 mixture of blue (type 1) and yellow (type 2) cells, the panels illustrate domain coarsening over time. (a) Early mixed state at $t = 10^3$ MCS. The inset shows a close-up of the red rectangle. (b) Intermediate state at $t = 4\times10^4$ MCS, showing emerging clusters. (c) Late stage at $t = 2\times10^6$ MCS, with well-separated rounded domains. Surface energies: $J_{11} = J_{22} = 8$, $J_{12} = 14$, $J_{2M} = 10$, and $J_{1M} = 22$.

By reproducing the main outcomes of the DAH, the CPM not only provided computational support for Steinberg's hypothesis but also established a flexible and extensible modeling platform. It has since been widely applied to investigate a broad range of morphogenetic processes, making it one of the most influential models in computational tissue biology.

1.1.2 Soft Disk Model

The Potts model is a powerful tool to test and verify many types of pattern formation in the cell segregation process. However, as it is an surface energy-based model, cell adhesion is an emergent property resulting from the minimization of energy at the interface between cells and the medium. In this sense, the model cannot demonstrate the Differential Adhesion Hypothesis (DAH) through direct and explicit mechanical interactions.

To address this issue, a new class of continuous, off-lattice models was developed. In a pioneering work, Belmonte et al. [44] proposed testing the DAH using an active soft disk model to represent individual cells. In this model, cells are represented as soft disks moving in a continuous space, and their interactions are governed by pairwise forces. The approach allows for an explicit test of the DAH by defining direct adhesion forces between cell centers, whose intensity depends on whether the interaction is homotypic (same cell type) or heterotypic (different types). This model was an extension of previous active matter models (the "boid" model) [8, 45], which were adapted to include cohesive interactions. Over the years, this approach has evolved, and other variations have been developed. Some subsequent models, for instance, use overdamped dynamics where forces directly determine the cell's velocity, rather than its orientation [30, 46–48]. Despite these

variations, the central principle of using pairwise forces to simulate adhesion remains, and the model's general structure can be summarized by a set of equations of motion:

$$\dot{\mathbf{r}}_i = \mu\,\mathbf{F}_{rand} + \mu \sum_j \mathbf{F}_{ij}, \tag{1.8}$$

where $\mu = 1/\gamma$ is the mobility, $\mathbf{F}_{rand}$ is a driven stochastic force (passive or active) and $\mathbf{F}_{ij}$ is the force exerted by neighbour j on cell i.

Each pair of cells i and j interacts through a short-range elastic repulsion and an elastic attraction. The total interaction force is given by:

$$\mathbf{F}_{ij}(t) = \begin{cases} -K_{rep}\,(r_{ij} - \sigma)\,\hat{\mathbf{r}}_{ij}, & r_{ij} < \sigma, \\ -K^{adh}_{\alpha\beta}\,(r_{ij} - \sigma)\,\hat{\mathbf{r}}_{ij}, & \sigma \le r_{ij} < l_{adh}, \\ 0, & r_{ij} \ge l_{adh}, \end{cases} \tag{1.9}$$

where $r_{ij} = \|\mathbf{r}_j - \mathbf{r}_i\|$ is the distance between cells, $\hat{\mathbf{r}}_{ij}$ is the unit vector from i to j, σ is the disk diameter, K_{rep} and $K^{adh}_{\alpha\beta}$ are the repulsive and attractive spring constants, respectively.

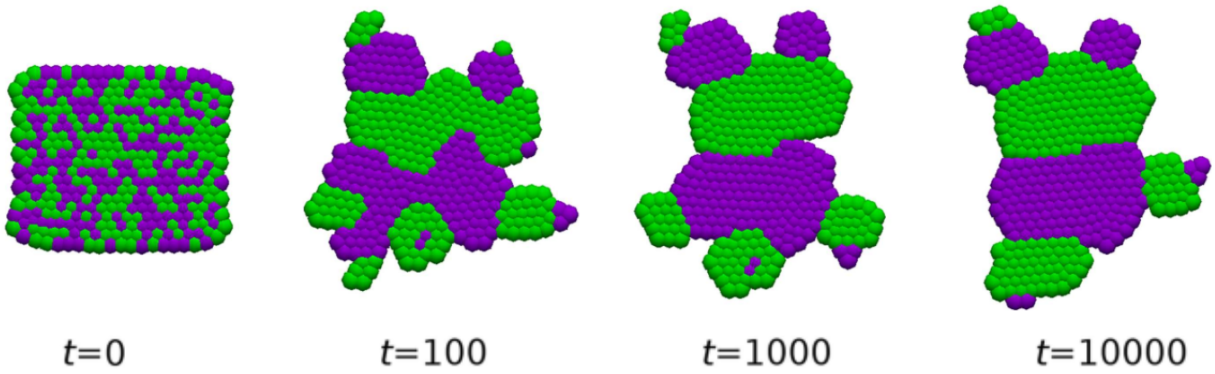

Figure 1.3: Figure adapted from Osborne et al. [47]. Spontaneous segregation of two cell types in a simulation of the soft disk model. The system evolves from a randomly mixed initial configuration to a sorted final state, in which like cells form cohesive domains.

Interactions vanish beyond a cut-off radius l_{adh}. In this model the adhesion interaction between cells of the type α and β are controled by $K^{adh}_{\alpha\beta}$. Therefore, the model explicit can test the Differential adhesion hypothesis. Molecular dynamics simulations using this model finds segregation when the heterotypic adhesion K_{12}, is smaller than homotypic adhesion K_{11} and K_{22}, yielding the condition

$$K^{\text{adh}}_{12} < \frac{K^{\text{adh}}_{11} + K^{\text{adh}}_{22}}{2}, \tag{1.10}$$

which is in agreement with DAH.

1.2 The Differential Interfacial Tension Hypothesis (DITH)

Building upon Steinberg's foundational ideas, a more comprehensive mechanical framework for cell segregation was developed in the early 2000s by Brodland [21]. This approach

aimed to elucidate the cellular factors responsible for generating surface or interfacial energies at cell–cell contacts. In Graner's approach, surface tension arises purely from differences in adhesion, which in turn define the surface energy. However, drawing on Harris's biologically grounded critique [14] of the Differential Adhesion Hypothesis (DAH), which we will examine in detail later, Brodland argued that interfacial tension is not solely a product of adhesion, but rather the net result of competing forces acting at the cell cortex and membrane:

- **Contractile Forces:** Generated by microfilaments in the cellular cortex (F_{MF}) and by the cell membrane itself (F_{Mem}), which tend to shorten the interface (see Fig. 1.4a-b).
- **Expansive Force:** Cell-cell adhesion (F_{Adh}) produced by specialized proteins, cadherins [15, 49], tend to elongate the interface (see Fig. 1.4a-b).

This distinction is crucial: adhesion acts in the opposite direction to the contractile components. The net interfacial tension (γ_{AB}) between two cells (A and B) is, therefore, the sum of these contributions (see Fig. 1.4b):

$$\gamma_{AB} = F_A^{Mem} + F_B^{Mem} + F_A^{MF} + F_B^{MF} - F_{AB}^{Adh} + F_{AB}^{Other}. \tag{1.11}$$

Thus, an increase in adhesion (F_{Adh}) reduces the net interfacial tension, diminishing the force available to shorten the boundary between the cells. This approach offers a more detailed mechanical explanation, incorporating both active contractions of the cytoskeleton and adhesion forces.

Furthermore, by employing the concept of interfacial tension, Brodland developed a mathematical framework that establishes criteria for the emergence of distinct spatial patterns in mixtures of cells. These criteria are derived from the mechanical balance of tensions acting at triple junctions, points where three cells or interfaces meet—and govern whether cells segregate, mix, or form checkerboard arrangements.

In Fig. 1.5a, we observe a typical triple junction involving three cells. When the heterotypic interfacial tension is greater than the homotypic one, i.e., $\gamma_{AB} > \gamma_{AA}$, the resulting net force displaces the junction toward the side of cell B. This movement favors the shortening of heterotypic interfaces and the expansion of homotypic contacts, which ultimately promotes the segregation of the two cell types. A symmetric argument for cell type B leads to the general condition for segregation:

$$\gamma_{AB} > \frac{\gamma_{AA} + \gamma_{BB}}{2} \quad \text{(Segregation)}. \tag{1.12}$$

Conversely, if the heterotypic tension is lower than the homotypic ones, such that $\gamma_{AB} < \gamma_{AA}$ and $\gamma_{AB} < \gamma_{BB}$, the triple junction shifts in a direction that increases heterotypic contacts. Under these conditions, cells of different types preferentially adhere to each other, leading to the formation of checkerboard-like patterns. The corresponding condition is simply the inverse inequality

$$\gamma_{AB} < \frac{\gamma_{AA} + \gamma_{BB}}{2} \quad \text{(Checkerboard)}. \tag{1.13}$$

This framework also extends to interfaces involving the external medium. In Fig. 1.5b, a triple junction is represented with two distinct cell types, A and B, in contact with the

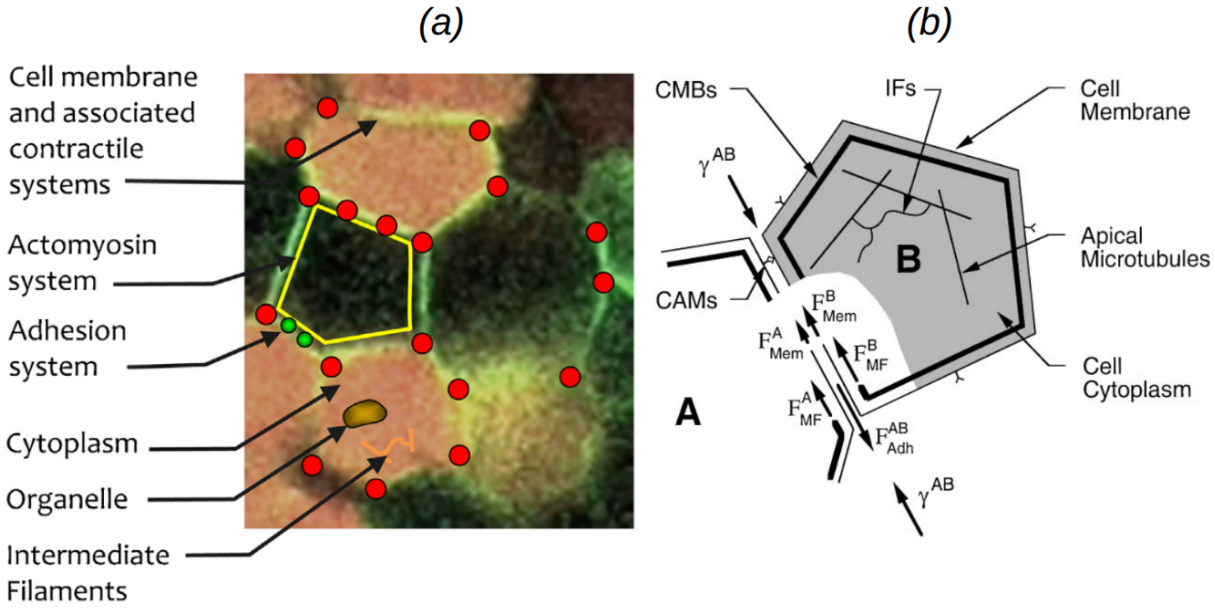

Figure 1.4: (a) Image of real epithelial cells. Figure adapted from Brodland [50]. (b) Schematic representation of a single cell, illustrating the primary force-generating elements. Contractile forces produced by circumferential microfilament bundles (CMBs) are denoted by $\mathbf{F}_{\text{CMB}}$, while those arising from the cell membrane and associated contractile proteins are grouped under $\mathbf{F}_{\text{mem}}$. Intercellular adhesion forces, arising from cell adhesion molecules (CAMs) and other junctional structures, are collectively represented by $\mathbf{F}_{\text{adh}}$, which tend to increase junction length. The cytoplasm and its network of intermediate filaments (IFs) are assumed to exert passive, viscous forces that modulate the dynamics of processes such as cell segregation and envelopment. Figure reproduced from Brodland et al. [51].

medium M. If the sum of the interfacial tensions along the AB and BM interfaces is smaller than that along the AM interface, the junction moves so that cell B contacts the medium and displaces cell A inward. In this scenario, cell A becomes engulfed by cell B. The condition for this to occur is:

$$\gamma_{AB} < \gamma_{AM} - \gamma_{BM} \quad \text{(Engulfment of A by B)}. \tag{1.14}$$

These conditions allow the Differential Interfacial Tension Hypothesis (DITH) to refine the segregation regimes initially proposed by the Differential Adhesion Hypothesis (DAH), while also accounting for behaviors that arise when contractility varies independently of adhesion. Since its formulation by Brodland, the DITH has become a central framework for explaining cell segregation [7, 18, 53] by emphasizing the net effect of cortical contractility and adhesion combined into a single mechanical quantity: the interfacial tension. Importantly, this model does not incorporate temperature, so the dynamics can become trapped in local energy minima. Over time, this hypothesis has been supported by a range of computational [21, 38, 50–52, 54, 55] and experimental approaches [4, 7, 18, 53]. Simulations based on line tension models—such as finite element methods [21, 50–52], Voronoi tessellations [47], and vertex-based [47, 54–57] frameworks, have consistently reproduced its predictions under diverse conditions. In parallel, measurements of tissue surface tension have confirmed its relevance in biological systems. Among the computational models incorporating the DITH, the vertex model has gained particular prominence for its ability

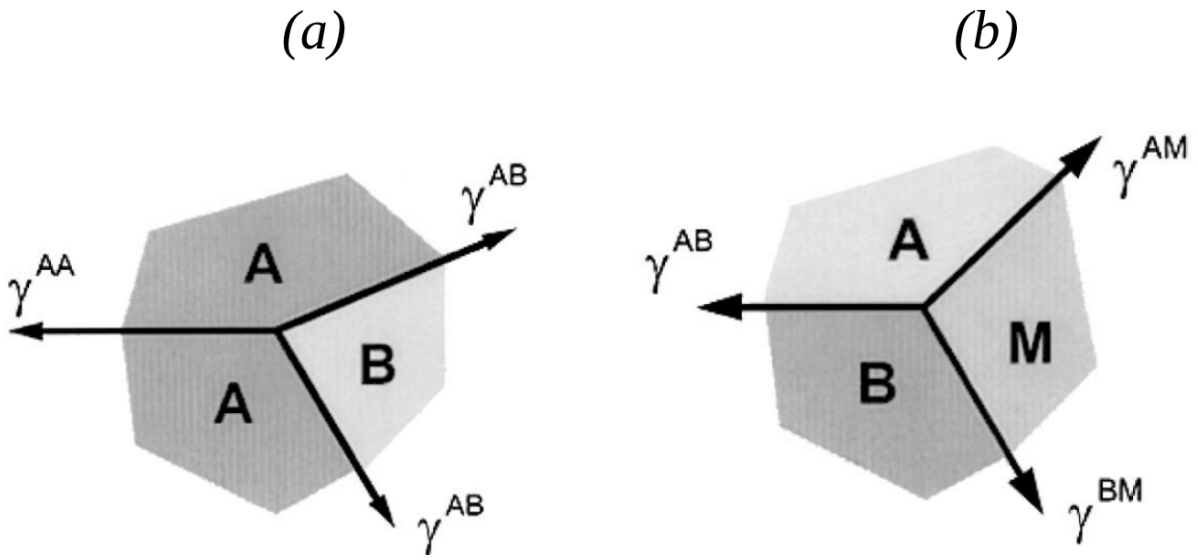

Figure 1.5: Figure adapted from Brodland [52]. Schematic representations of triple junctions illustrating the mechanical basis of cell segregation and envelopment, as predicted by the Differential Interfacial Tension Hypothesis (DITH). (a) Triple junction involving three cells, used to derive the condition for segregation. When the heterotypic tension γ_{AB} exceeds the average of the homotypic tensions, the junction reorients to favor homotypic contacts, leading to cell segregation. (b) Triple junction involving two cell types, A and B, in contact with the external medium M. When the condition $\gamma_{AB} + \gamma_{BM} < \gamma_{AM}$ is satisfied, cell A is displaced inward and engulfed by cell B, establishing a mechanical criterion for tissue-level envelopment.

to capture cell geometry, interfacial mechanics, and topological rearrangements in a cohesive framework. The next section presents segregation results obtained with this model, illustrating how the DITH can be directly implemented and explored.

1.2.1 The Vertex Model (VM)

The Vertex Model (VM) [47, 54–58] is one of the most widely used and conceptually elegant frameworks for modeling confluent epithelial monolayers. Originally derived from foam physics, the VM represents epithelial tissues as a two-dimensional tessellation of convex polygons (see Fig.1.6). Each polygon corresponds to a cell; edges represent cell-cell junctions, and vertices mark points where three or more cells meet (see Fig.1.6). The model assumes that cells are approximately of equal height, so that tissue mechanics can be effectively captured in two dimensions.

The VM offers a compact and geometrically explicit description of epithelial structure and has proven particularly effective in studying processes such as tissue elongation, cell rearrangements (T1 transitions), topological defects, and cell segregation. Notably, it has also been employed to simulate *cell segregation* and to test the *Differential Interfacial Tension Hypothesis* (DITH) by incorporating heterotypic and homotypic tension differences. Its popularity stems from its balance between computational efficiency and the ability to capture complex mechanical and topological features of tissues. Over the past two decades, numerous studies have extended the model to incorporate active forces [55], anisotropies [59, 60], and interfacial tension differences [55, 60] making it a versatile tool

for investigating a wide range of epithelial phenomena.

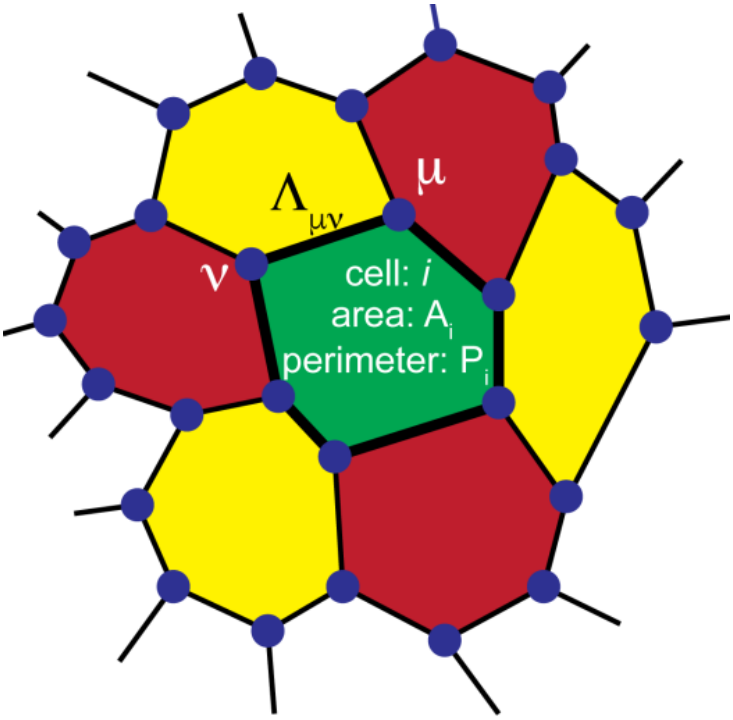

Figure 1.6: Figure reproduced from [55]. Schematic representation of the Vertex Model. Cells are polygons that tile the plane without gaps or overlaps. Each vertex (dark blue dot) is the intersection of three edges (junctions). Each cell is characterized by a reference area A_0, area modulus K_A, perimeter modulus K_P, and the interfacial tension $\Lambda_{\mu\nu}$ along junctions.

In the VM, the energy function of a tissue configuration is given by:

$$E = \sum_{i=1}^{N} \left[\frac{K_A}{2}(A_i - A_0)^2 + \frac{K_P}{2}(P_i - P_0)^2 \right] + \sum_{\langle \mu,\nu \rangle} \Lambda_{\mu\nu} \ell_{\mu\nu}, \tag{1.15}$$

where:

- N is the number of cells,
- A_i and P_i are the area and perimeter of cell i,
- A_0 and P_0 are its preferred area and perimeter respectively,
- K_A and K_P are its area and perimeter elastic moduli,
- $\ell_{\mu\nu}$ is the length of the edge (junction) between vertices μ and ν,
- $\Lambda_{\mu\nu}$ is the interfacial tension along that junction.

The dynamics of the system is usually described in the overdamped limit, where inertia is negligible. Vertex positions $\mathbf{r}_\mu$ evolve according to:

$$\gamma \dot{\mathbf{r}}_\mu = -\nabla_\mu E, \tag{1.16}$$

where γ is the viscosity. The resulting system of coupled nonlinear ODEs is solved numerically using molecular dynamics. For binary mixtures of cells, the interfacial (junction) tension $\Lambda_{\mu\nu}$ is typically defined for each pair of cell-cell and cell–boundary contacts $\Lambda_{\alpha\beta}$. The energy function can then be written as:

$$E = \sum_{i=1}^{N} \left[\frac{K_A}{2}(A_i - A_0)^2 + \frac{K_P}{2}(P_i - P_0)^2 \right] + \sum_{\langle \mu,\nu \rangle} \Lambda_{\alpha\beta}\, \ell_{\mu\nu}, \tag{1.17}$$

where the interfacial tension between vertices μ and ν depends on the identity of the neighboring cells or boundaries, labeled by α and β. Since the vertex model assumes

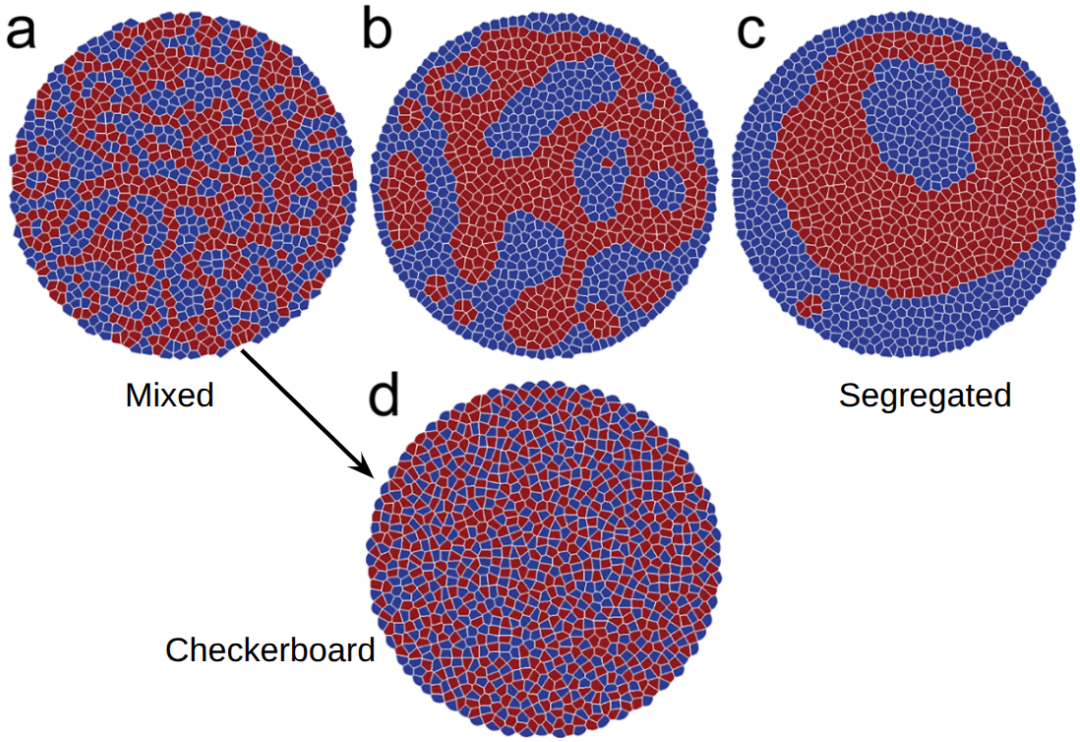

Figure 1.7: Figure adapted from Barton et al. [55]. (a–c) Snapshots of a two-cell-type system at times $t = 10$, 500, and 5000, where type 1 cells are shown in blue and type 2 cells in red. Interfacial tensions are set to $\Lambda_{11} = -6.8$, $\Lambda_{22} = -6.2$, $\Lambda_{12} = -6.4$, and $\Lambda_{1M} = \Lambda_{2M} = -6.2$. (d) A checkerboard-like pattern rapidly emerges (already visible at $t = 10$) when heterotypic (red–blue) interfaces become energetically more favorable than homotypic ones. This occurs for $\Lambda_{12} = -6.7$, with all other tensions unchanged.

overdamped dynamics, the system remains immobile in the absence of external driving forces. Therefore, in dynamical simulations, a random driving force is typically added to the equation of motion:

$$\gamma \dot{\mathbf{r}}_\mu = \mathbf{F}_{\text{drive}} - \nabla_\mu E, \tag{1.18}$$

where $\mathbf{F}_{\text{drive}}$ is a stochastic driving force acting on all vertices (including μ) of a given cell. This force can represent either passive Brownian noise [47] or an active self-propulsion direction [55]. Simulations with the vertex model, similar to the Potts model, exhibit distinct pattern formation depending on the energetic cost of forming interfaces. Typical interfaces l_0 with lower interfacial energy $E_\Lambda \sim \Lambda\, l_0$ are more likely to form, leading to outcomes such as segregation between types 1 (blue) and 2 (red), or engulfment of one cell

type by another (see Fig. 1.7c). When heterotypic interfaces are energetically preferred, a checkerboard pattern emerges (see Fig. 1.7d).

These different regimes appear by varying the relative interfacial tensions, and the model has been widely used and verifying the conditions predicted by the DITH proposed by Brodland (see captions of Fig. 1.7), such as

$$\Lambda_{12} > \frac{\Lambda_{11} + \Lambda_{22}}{2}, \qquad \text{(segregation)} \tag{1.19}$$

$$\Lambda_{12} < \frac{\Lambda_{11} + \Lambda_{22}}{2}, \qquad \text{(checkerboard pattern)} \tag{1.20}$$

$$\Lambda_{12} < (\Lambda_{1M} - \Lambda_{2M}), \qquad \text{(engulfment of type 1 by type 2)} \tag{1.21}$$

where Λ_{1M} and Λ_{2M} are the interfacial tensions between cells of type 1 and type 2 with the medium, respectively.

1.3 Differential Surface Contraction Hypothesis (DSCH)

The Differential Adhesion Hypothesis (DAH) has long served as a foundational framework for explaining cell segregation and tissue organization. It establishes that passive differences in interfacial adhesion energies between cells are sufficient to drive segregation, in analogy with the thermodynamic behavior of immiscible fluids. Over time, this concept was generalized into the Differential Interfacial Tension Hypothesis (DITH), which treats interfacial tension as an emergent property arising from both adhesive and contractile contributions at cell–cell interfaces. While this unified approach has proven useful for modeling a variety of morphogenetic phenomena, it has also raised important questions about the specific mechanical forces driving tissue patterning.

New experimental and theoretical evidence increasingly challenges the notion that adhesion alone can explain the complex behaviors observed in living tissues [4, 7, 61]. In particular, actively generated contractile forces, especially those mediated by the actomyosin cortex, have emerged as critical and previously underappreciated determinants of tissue mechanics and spatial organization. In the 1970s, Harris [14] offered a pioneering critique of the adhesion view and introduced the Differential Surface Contraction Hypothesis (DSCH). This hypothesis shifts the focus from passive adhesion to the active regulation of surface tension by cytoskeletal contractility as a principal mechanism for driving cell segregation and morphogenesis. Based on evidence of cortical actin-like filament layers observed during developmental processes such as invagination, neurulation, and tissue internalization, Harris proposed that differences in surface contractility, actively generated by the cytoskeleton, govern the spatial organization of heterogeneous cell populations.

The DSCH rests on two core assumptions:

(a) Surface contractility is highest at the cell–medium interface, lowest at homotypic cell–cell contacts, and intermediate at heterotypic interfaces;

(b) Cells from different types exhibit distinct levels of surface contractility with the medium.

From these premises, it follows that in a binary mixture, the more contractile cell type should relocate to the interior of the aggregate to minimize its exposed surface and reduce

its overall mechanical energy. Importantly, the DSCH does not reject the relevance of adhesion-based mechanisms but challenges their sufficiency, highlighting instead the role of cortical tension as a central and actively regulated driver of cell segregation.

Notably, the DSCH is also consistent with the mathematical criteria for pattern formation proposed by Brodland [21], who analyzed force balances at triple junctions and demonstrated that stable segregation requires asymmetries in interfacial tensions between distinct cell types. In this framework, spatial patterning emerges when force vectors at junctions fail to cancel out unless homotypic contacts are maximized. The DSCH provides a mechanistic foundation for this behavior by linking such asymmetries to differences in active cortical contractility, offering a dynamic and cell-intrinsic explanation for the physical conditions underlying domain formation.

Key Experimental Evidence Supporting the DSCH

Several experimental studies have provided direct support for the DSCH by showing that differences in cortical contractility, independent of differential adhesion, are sufficient to drive cell segregation. Notably, Krieg et al. [4] demonstrated that ectodermal cells in zebrafish embryos exhibit higher cortical tension than mesodermal cells, and that this difference governs their spatial positioning within aggregates: the more contractile ectoderm consistently sorted to the interior (see Fig. 1.8a-d) .

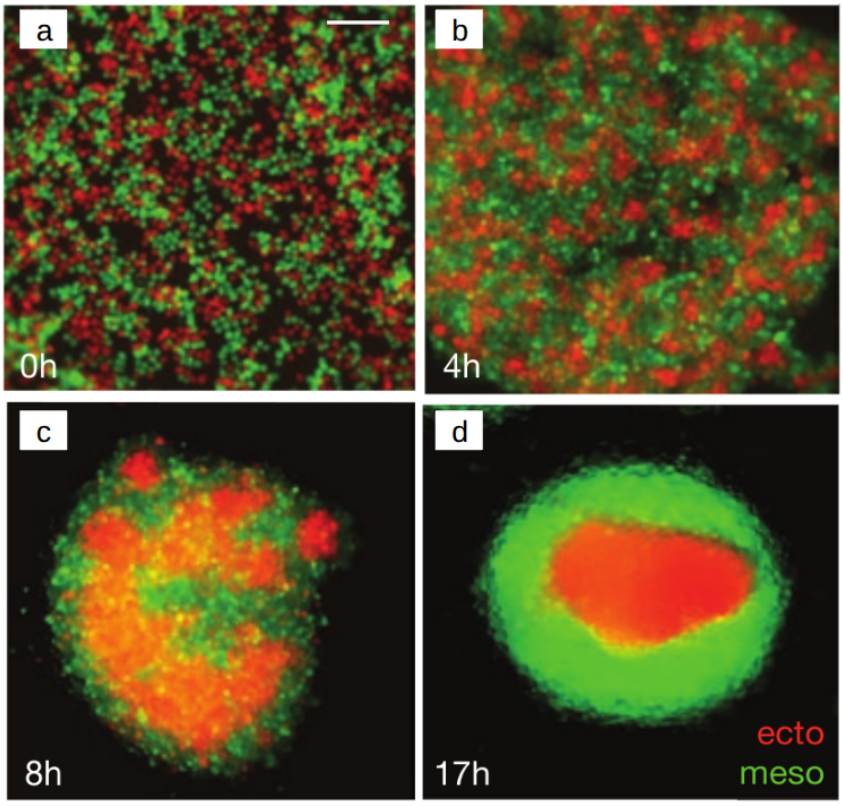

Figure 1.8: Figure adapted from Krieg et al. [4]. (a-d) Time-lapse images showing the segregation dynamics of mesoderm and ectoderm progenitor cells in co-culture. Ectoderm cells, which exhibit higher actomyosin-dependent cortical tension, relocate to the interior of the heterotypic aggregate. This behavior suggests that cortical tension, rather than differential cohesion, is the primary driver of progenitor segregation to the inside.

Skamrahl et al. [61] further reported that early segregation in epithelial co-cultures

arises from intrinsic asymmetries in actomyosin contractility, with minimal contribution from differential adhesion, while Méhes et al. [7] demonstrated that targeted manipulation of contractility alone can invert segregation geometry, confirming cortical tension as a primary regulator of tissue organization. O'Neill et al. [62] provided direct evidence that cell segregation can be driven by differential cortical contractility alone: working with ephrin-B1 mosaic mouse embryos and heterotypic co-cultures, they showed that unidirectional, kinase-dependent EphB forward signaling triggers ROCK activation, producing a localized increase in actomyosin tension in EphB2-expressing cells sufficient to drive segregation without adhesion differences. Kindberg et al. [63] further reinforced this conclusion using engineered embryonic stem cell systems and in vivo analysis of the mouse midbrain-hindbrain boundary, demonstrating that ROCK-dependent increases in cortical tension at heterotypic contacts are not only sufficient to produce sharp and stable tissue boundaries, but also remain effective when cell-cell adhesion is experimentally held constant. Collectively, these findings validate the central assumptions of the DSCH and highlight active contractility as a sufficient and robust physical mechanism for pattern formation, in full agreement with the original hypothesis proposed by Harris.

1.3.1 Ring-Membrane Model: Active Rings with Differential Contraction

Despite its conceptual clarity and increasing experimental support, the Differential Surface Contraction Hypothesis (DSCH) remains largely unexplored in computational studies that isolate contractility as the sole driving mechanism of cell segregation. Most existing frameworks, such as the Cellular Potts model, vertex-based formulations, and finite element methods represent interfacial forces using effective energy terms that combine adhesion and contractility into a single parameter. While this approach can reproduce many morphogenetic patterns, it obscures the individual roles of adhesion and surface tension, making it impossible to disentangle their respective contributions. In addition, these models typically idealize cell shapes and lack an explicit representation of the cellular membrane, which plays a central role in controlling mechanical interactions.

To overcome these limitations and directly test the original hypothesis proposed by Harris [14], we developed a novel membrane-based model in which each cell is represented as a ring [64–66]. This ring is composed by active soft disks connected by springs, forming a closed loop that mimics the mechanical properties of a contractile cell cortex (see Fig.1.9). The model explicitly incorporates a contact-dependent contraction mechanism that activates only when neighboring rings come into proximity, allowing precise control of cortical tension at homotypic, heterotypic, and cell–medium interfaces (see Fig.1.9). Adhesion parameters are held fixed and identical for all cell types, ensuring that any emergent segregation arises solely from differences in surface contractility.

This framework captures the essential principles of the DSCH and enables, for the first time, a controlled in silico investigation of segregation driven **exclusively** by differential surface contraction. Moreover, it provides a flexible platform to simulate multicellular systems with dynamic shape fluctuations, directional motion, and tunable mechanical responses, key features of real biological tissues.

The model builds upon previous work on passive elastic rings [67, 68] and extends our earlier efforts [65, 66] by introducing activity and local contractility. The inclusion of a tunable surface contraction rule is the key innovation that allows us to isolate the DSCH from adhesion-based effects, fulfilling a long-standing need in the field of computational

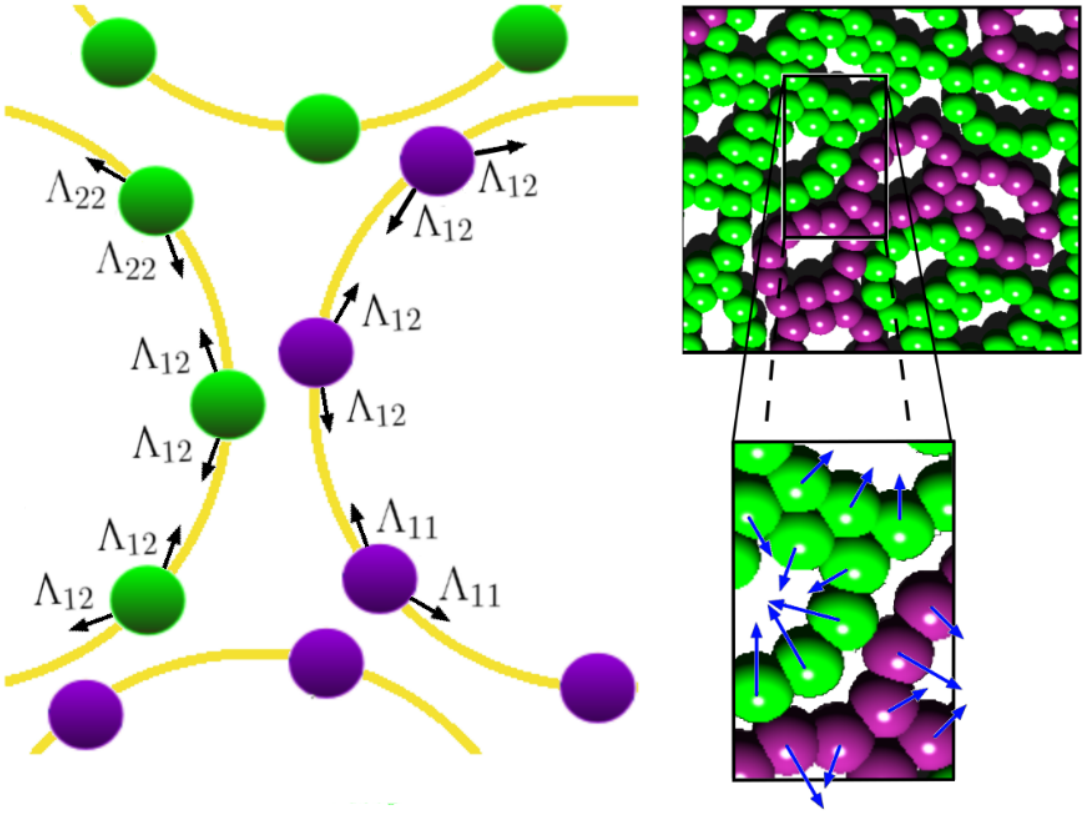

Figure 1.9: Schematic of the active ring model introduced in this work [64]. Each cell is modeled as a closed elastic ring composed of active particles connected by springs. Contractile interactions arise only when particles from different rings are within a cut-off distance l_Λ, generating forces (red arrows) that locally straighten the membranes. These forces depend on the ring types, allowing differential contraction at homotypic, heterotypic, and cell–medium interfaces. This setup enables the explicit and independent control of surface tension, isolating its effects from adhesion.

Table 1.1: Capability of different computational models to test mechanical hypotheses of cell segregation. We distinguish between **explicit** testing, where a mechanism is directly implemented and independently controlled, and **implicit** testing, where it is embedded in effective or combined terms.

Computational Model	**DAH**	**DITH**	**DSCH**
Potts Model (CPM)	Implicit	Explicit	Implicit
Soft disks	Explicit	No	No
Voronoi Tessellation	Implicit	Explicit	Implicit
Vertex Model	Implicit	Explicit	Implicit
Finite Element Method (FEM)	Implicit	Explicit	Implicit
Rings (this work)	Explicit	Explicit	**Explicit**

tissue mechanics.

As summarized in Table 1.1, most existing models are only capable of testing the DAH and DITH in an implicit or hybrid manner. The active ring model introduced in this work is, to our knowledge, the first to implement all three hypotheses: DAH, DITH,

and DSCH with explicit and independently tunable mechanisms. This capability forms the central methodological contribution of this thesis and offers a new computational tool for dissecting the mechanical basis of cell segregation.

The main results obtained with this model were published in Physical Review Letters [64]. In this thesis, these results are presented in Chapter 2. The publication is available online at: https://journals.aps.org/prl/abstract/10.1103/PhysRevLett.134.138401.

Chapter 2

Article: Segregation in binary mixture with differential contraction among active rings

Segregation in binary mixture with differential contraction among active rings

Emanuel F. Teixeira,[1,*] Carine P. Beatrici,[1,†] Heitor C. M. Fernandes,[1,‡] and Leonardo G. Brunnet[1,§]

[1] *Instituto de Física, Universidade Federal do Rio Grande do Sul, CP 15051, CEP 91501-970 Porto Alegre - RS, Brazil*

(Dated: March 6, 2025)

Cell cortex contraction is vital for shaping cells, enabling movement, division, and responding to mechanical signals—processes crucial for multicellular organisms. Differential membrane contractions between cells significantly influence segregation. We present a model where active particle rings interact through differential contraction, showing that segregation arises from this mechanism, with ring activity functioning as an effective temperature. The interface decay exponent is close to $\lambda \sim 1/3$, differing from previous cluster fusion/diffusion model predictions.

In cellular systems made up of different species, sorting is a common emergent behavior. During embryonic development, cells undergo differentiation, which leads to the segregation of cell types in tissue formation. Based on experimental evidence [1–4] and motivated by physical systems like binary mixtures, where spontaneous separation of two liquids is observed, Steinberg proposes [5] that the mechanism for cell segregation lies in the difference in adhesion between cells of different types. This proposal became known as the Differential Adhesion Hypothesis (DAH) or Steinberg Hypothesis.

Harris [6] questions the foundation of the DAH hypothesis, highlighting that maximization of intercellular adhesion does not necessarily lead to the observed effects of cell sorting. He suggested that within a heterogeneous cell aggregate, variation in surface contraction, driven by the active regulation of the acto-myosin cortex, could be the driving force behind tissue engulfment and cell sorting in vivo. The surface contraction of a particular cell appearing more pronounced when it comes into contact with a cell of a different type. Besides that, cells from different tissues exert different surface contraction when contacting the medium. This sorting mechanism was named Differential Surface Contraction Hypothesis (DSCH).

In line with Harris's ideas, Brodland [7] successfully described segregation using finite element simulations that incorporated adhesion and surface contractions, both contributing to the total interfacial tension, a mechanism known as differential interfacial tension hypothesis (DITH). In fact, these hypotheses have been tested using various other extended numerical models, including Cellular Potts [8–13] and Vertex models[14–17]. All theses models define an effective interfacial tension between different units but do not explicitly separate adjacent cell membranes or detail the forces involved, such as adhesion and surface contraction. However, from an experimental perspective, the role of membrane fluctuations was clearly highlighted by Mombach [18], and the distinction between adhesion and cortical tension was emphasized in the work of Krieg et al.[10] and Manning et al. [19].

In this work, we present a model of active rings interacting through differential membrane contraction when within a specific cutoff distance. By utilizing two interacting membranes, this model provides a more detailed representation of biological processes, offering insights into how different layers interact and differentiating the roles of fluctuations, adhesion, and cortex contraction. To our knowledge, this is the first time Harris's mechanism has been simulated in isolation.

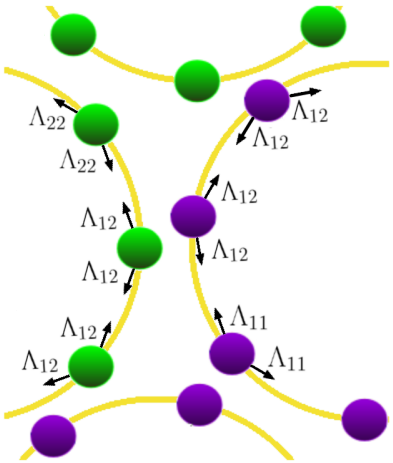

FIG. 1. Active ring model. Contractions occur when two particles from different rings are within a distance l_Λ. The resulting force tends to straighten the membrane.

Boromand and collaborators [20, 21] introduced a ring system composed of passive particles connected by springs. Building on this model, we incorporated active properties into the particles forming the ring in previous articles [22, 23]. We model a 2D system with N rings, each representing a cell formed by n active particles (see Fig. 1). The system is set up as a binary mixture of active rings confined in a circular arena with repulsive walls and radius R_0. The set of coupled overdamped equations governing the dynamics of each particle are: $\dot{\mathbf{r}}_{i,j} = v_0\ \mathbf{n}_j - \mu\,\mathbf{F}_{i,j}$ and $\dot{\mathbf{n}}_j = \sqrt{2\,D_R}\ \boldsymbol{\xi}_j \times \mathbf{n}_j$, where $\mathbf{r}_{i,j}$ denotes the position of the i-th particle within the j-th ring at time t, μ represents its mobility and v_0 is the

magnitude of active velocity with its orientation given by $\mathbf{n}_j$. The second term, $\mathbf{F}_{i,j} = -\boldsymbol{\nabla}_{i,j} E$ represents the total force acting on the i-th particle within the j-th ring. The direction of the active force, described by unit vector $\mathbf{n}_j$, experiences angular Gaussian white noise $\boldsymbol{\xi}_j = \xi_j \hat{e}_z$ with correlation $\langle \xi_j(t_1)\xi_k(t_2)\rangle = \delta_{jk}\delta(t_1 - t_2)$. The noise term D_R represents the rotational diffusion coefficient, which defines a characteristic timescale given by $\tau_R = 1/D_R$.

The energy function has contributions from (i) a perimeter energy (springs connecting ring neighboring particles), (ii) area conservation, (iii) contact-dependent contraction term, (iv) core repulsion among non-neighboring particles from any ring and inter-cellular adhesion,

$$E = \sum_{j=1}^{N} \left\{ \frac{\epsilon_P}{2} \sum_{i=1}^{n} \left(\frac{|\vec{l}_{i,j}|}{l_0} - 1 \right)^2 + \frac{\epsilon_A}{2} \left(\frac{A_j}{A_0} - 1 \right)^2 + \sum_{i=1}^{n} \Lambda_{\alpha\beta} |\vec{l}_{i,j}| \right\} + \frac{\epsilon_c}{2} \sum_{r_{ik} \le \sigma} \left(\frac{r_{ik}}{\sigma} - 1 \right)^2 + \frac{\epsilon_{adh}}{2} \sum_{\sigma < r_{ik} \le l_{adh}} \left(\frac{r_{ik}}{\sigma} - 1 \right)^2, \quad (1)$$

where $\vec{l}_{i,j} = \vec{r}_{i,j} - \vec{r}_{i-1,j}$ is the vector connecting consecutive particles in ring j, ϵ_P is the elastic energy of the spring controlling perimeter fluctuations, and l_0 is the equilibrium distance in the ring. The elastic energy related to area control is ϵ_A, A_j is the inner area of the j-th ring (not considering the area of particles), and A_0 is the equilibrium area. The last two terms in Eq. 1 represent the core repulsion between non-neighboring particles and the adhesion between particles of different rings, respectively. Parameter ϵ_c denotes the characteristic energy of the core repulsion interaction, while r_{ik} is the distance between particles i and k. The equilibrium cut-off distance, σ, effectively defines the particle diameter. The adhesion energy and interaction distance are characterized by ϵ_{adh} and l_{adh}, respectively.

A key distinction between the ring model and other extensive models (Finite Elements [7] and Vertex-Voronoi model [14–17, 24, 25]) lies in the rings contact interface, which comprises two contact membranes. This bring us to the third term in Eq. 1 which incorporates differential surface contraction. In this term, parameter Λ_{11} represents the line tension between particles belonging to type 1 rings (purple rings in Fig. 1), Λ_{22} represents the line tension between type 2 rings and $\Lambda_{12} = \Lambda_{21}$ represents the line tension between rings of different types. All these tensions acting when they are within a cutoff distance l_Λ. A central parameter in this work is $\Lambda = \Lambda_{12}/\bar{\Lambda}$, with $\bar{\Lambda} \equiv (\Lambda_{11} + \Lambda_{22})/2$. We set $\Lambda_{11} = \Lambda_{22} = 0.5$, hence Λ_{12} varies within the range $[0.05 : 5]$.

These tensions result in a force on a ring particle that straightens the interface, acting as an external force on that particle, without affecting its neighbors. Consequently, there is no conservation of momentum for the ring as a whole. Nevertheless, due to the symmetric value of Λ_{ij} $(i = 1, 2;\ j = 1, 2)$, the same force will also act on the corresponding particle in the other ring. Therefore, for this particular symmetric case, Newton's third law is applicable to the pair of rings. However, in living systems, interactions aren't always reciprocal [26–29]. Fig. 1 shows a schematic representation of the active ring system, illustrating the involved tensions.

To handle the interaction with the walls, which can be seen as the medium in our context, we specify that the particles of a ring increase their contraction tension once they reach a distance $\sigma/2$ from the wall. This prevents the rings from preferring to accumulate on the wall. The contraction between rings of type 1 (purple) and the "medium" (wall) is defined as $\Lambda_{1M}/\bar{\Lambda} = 12$, while for rings of type 2 (green), we use $\Lambda_{2M}/\bar{\Lambda} = 0$. This choice satisfies the criterion $\Lambda_{12} < \Lambda_{1M} - \Lambda_{2M}$ (valid for all values of Λ_{12} in this work) for the engulfment of one type (purple) by the other (green) [7, 14].

We measure spatial coordinates and time in units of l_0 and τ_R, respectively. As a result, the model equations may be written in terms of the Péclet number [30, 31], defined as $Pe \equiv \frac{v_0 \tau_R}{l_0}$, which controls the level of activity. The system remains in the liquid phase due to the chosen Péclet number $(0.1 < Pe < 0.7)$ and shape index $p_0 = \frac{n l_0}{\sqrt{A_0}} = 4$, [20]. Details of the numerical integration method and the remaining parameter values are provided in the Supplemental Material [32].

We begin our simulations with an initial random distribution of rings (see Fig. 2a). For $\Lambda > 1$, we observe a spontaneous segregation process among the rings, with larger Λ values resulting in a smaller interface between ring types, indicating improved segregation. This is illustrated at the bottom of Fig. 2a, where $\Lambda = 10$. (See video 3 in Supplemental Material [32]). For $\Lambda = 1.5$ (middle of Fig. 2a), the system still segregates, but a larger asymptotic interface remains. (See video 2 in Supplemental Material [32]). In contrast, for $\Lambda < 1$ (top of Fig. 2a), an organized mixed state emerges, forming a checkerboard-like pattern where each ring tends to be in contact with a ring of a different type. (See video 1 in Supplemental Material [32]).

To quantify the level of segregation in the system, we use the parameter γ, as introduced by Belmonte and collaborators [33]. This parameter is defined as the mean fraction of neighboring rings of type 2 (green) surrounding rings of type 1 (purple): $\gamma = \left\langle \frac{n_2}{n_1+n_2} \right\rangle_1$, where $\langle .. \rangle_1$ denotes the average over all rings of type 1, with n_1 and n_2 representing the number of first neighbors of type 1 and type 2, respectively. In the literature, it is well established that the segregation parameter is directly correlated with the interface I between the types, expressed as $\gamma \sim I$ [34, 35].

We examined the evolution of the segregation param-

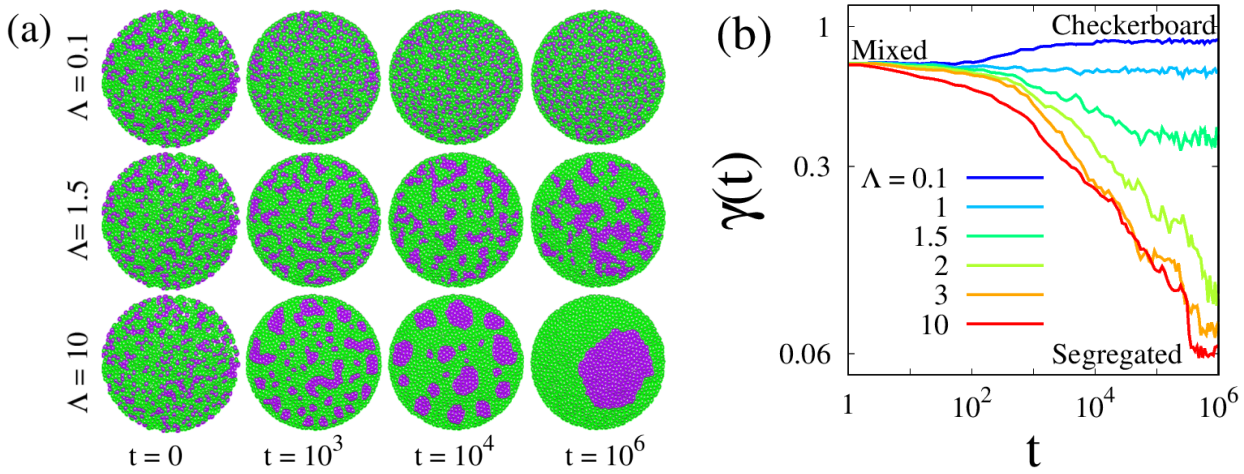

FIG. 2. (a) Snapshots of a binary mixture of rings for various values of Λ. For Λ = 10 (bottom), a stable segregation state emerges, where all clusters eventually merge into a final configuration with a single cluster of the minority type (purple rings). For Λ = 1.5 (center), cluster formation begins but remains unstable, with clusters continuously breaking apart. For Λ = 0.1 (top), system transitions from an initially mixed state to a configuration where rings contact those of a different type, in a checkerboard-like pattern. b) Time series of the segregation parameter for various differential contractions Λ. System begins in a random configuration with 30% purple rings and 70% green rings.

eter γ for various Λ values while keeping the Pe value fixed. As shown in Fig. 2b), the asymptotic value of γ reaches low levels (approximately $\gamma \sim 0.1$ with 10^3 rings) for the segregated state and increases to $\gamma \sim 0.9$ as Λ decreases. The line separating the segregated and checkerboard patterns occurs at $\Lambda \sim 1$, where the initial value of the mixed state ($\gamma \sim 0.7$) is maintained throughout the evolution.

Furthermore, we measured mean values of steady-state γ as a function of Λ for several values of Pe (see Fig. 3a). Here we emphasize the role of parameter Pe, which broadens the transition as its value increases, and the importance of initial configurations to avoid stay trapped in a meta-stable state. While at low Pe values ($Pe \leq 0.2$ in Fig. 3a) and $\Lambda < 1$, the system evolves to the checkerboard pattern, for $\Lambda > 1$ it remains trapped close to the initial configuration, so we employed the segregated state as the initial condition to test the effect of Pe. In brief, Pe functions like temperature, enabling the system to overcome potential barriers to approach the minimum energy state. Simultaneously, it is responsible for deviating from the optimal value due to the introduced fluctuations.

In Fig. 3b we present a ($\Lambda \times Pe$) diagram, colors indicate the mean value for γ. At low Pe values, the segregation region occurs just above $\Lambda = 1$, but at high activity we observe a mixed state well above this limit. This indicates that the segregation criterion [7, 14] $\Lambda_{12} > (\Lambda_{11} + \Lambda_{22})/2$ is only valid at low Pe. Similar arguments apply to the checkerboard state in the region defined by $\Lambda < 1$.

Additionally, we conducted an analysis similar to previous works [36] and observed how the steady state of largest cluster of type 1 rings (purple) changes with Pe

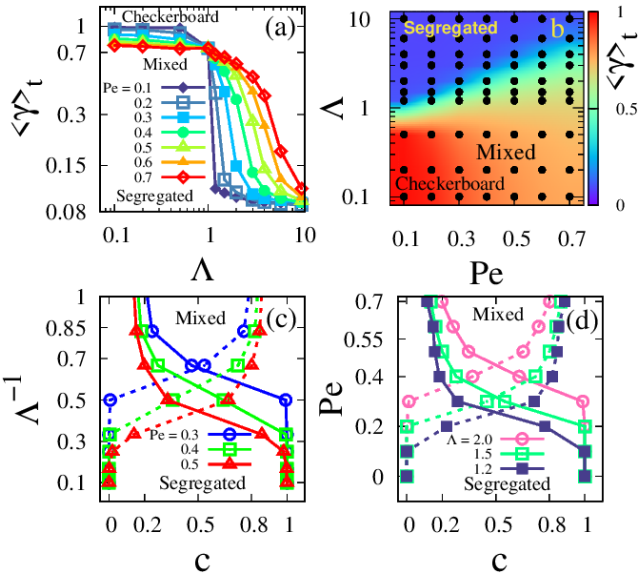

FIG. 3. (a) Steady-state mean values of segregation parameter γ as a function of Λ for various values of Pe. (b) Diagram ($Pe \times \Lambda$) that separates checkerboard, mixed and segregated regions. Colors represent the average values of segregation parameter for long times. (c) Binodal curves from the concentration c of rings of type 1 (purple ones) inside the largest cluster c_{in} and outside c_{out} (dashed lines) for three values of Pe. See text for details. (d) Binodal curves from the concentration c of rings of type 1 (purple ones) inside the largest mean cluster c_{in} and outside c_{out} (dashed lines) for three values of Λ. See text for details. Fixed parameter: $N = 500$.

and Λ. We define the fraction of these rings that are inside the largest cluster as $c_{in} = N_{int}/N_1$. N_1 and N_{int} are the total number of type 1 rings and the number of rings in the largest asymptotic cluster, correspondingly. Using $c_{out} = 1 - c_{in}$, we can construct a binodal curve that delineates regions of segregation and mixing as function of Λ^{-1} and Pe (see Figures 3c-d). Below the intersection we have the segregated state ($c_{in} \sim 1$ and $c_{out} \sim 0$, one large cluster) and above, the mixed state (several clusters of similar size). Fig. 3d shows the effect of the activity parameter Pe on the binodal curves. Depending on the value of Λ, there is a value of Pe beyond which the system transitions from segregated to mixed state.

Our focus now shifts to understanding how the system evolves from a randomly mixed configuration to a segregated one. This is particularly important because the long time behavior before saturation of the segregation parameter and the mean size growth of clusters can provide information about the underlying mechanisms occurring during tissue formation. The mean cluster's size of rings of type 1, $M(t)$, is obtained using the cluster-counting algorithm used by Beatrici et al. [34]. Here, we analyze the case where contact between different rings type is unfavorable ($\Lambda = 10$). Initially, the system is in a mixed configuration with a corresponding value of $\gamma \equiv \gamma_0 = 0.7$, consequent of the (30:70) proportion of ring types. In Fig. 4a, we show the evolution of the segregation parameter normalized by its initial value, $\bar{\gamma}(t) = \gamma(t)/\gamma_0$. The activity Pe determines the duration of the transient period, with higher activity implying shorter transients. Subsequently we observe an algebric decay, $\gamma \sim t^{\lambda}$ with an exponent close to $-1/3$ for at least two decades, independent of the activity value Pe. Additionally, in this regime, the mean domain size M grows with an exponent close to $2/3$ (see Fig. 4c). Thus, we observe an inverse relationship, $\gamma \sim M^{-2}$, consistent with previous findings [11, 13, 17, 35].

In Fig. 4b, we observe that significantly unequal proportions slow down the domain growth process, as it relies on the coalescence of minority clusters diffusing within the majority type.(See video 4 in Supplemental Material [32]). However, when the proportions are equal (50:50), the dynamics change — the system quickly percolates, and the process of interface reduction becomes dominated by rounding. In this case, we expect exponent $\sim -1/2$ [37]. For other proportions, we observe asymptotic time exponents close to $-1/3$ and $2/3$ for γ and M, respectively, while maintaining the inverse relationship, $\gamma \sim M^{-2}$ (see Fig. 4b-d).

In conclusion, we present a model where cells are represented by rings of active particles. Each ring being explicitly equipped with its own membrane, allowing it to accommodate negative curvatures and replicate all cell sorting mechanisms, whether in isolation or combined. This represents a significant advancement in the class of extended cell models, offering a path to more realistic depiction of cell behavior as observed in experiments.

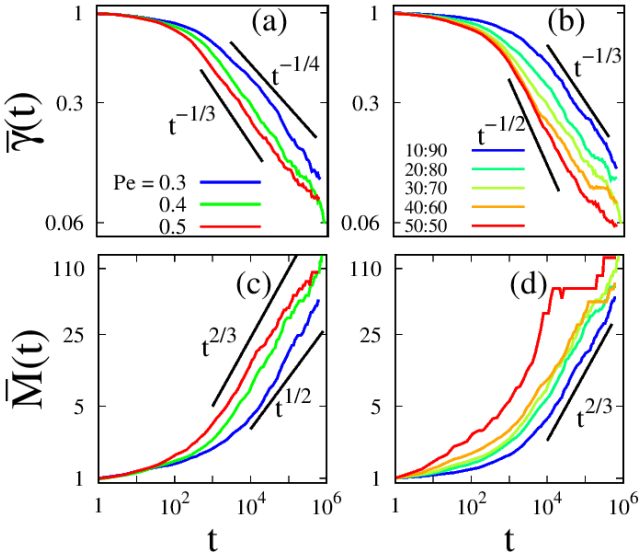

FIG. 4. (a) Evolution of the rescaled segregation parameter $\bar{\gamma}(t) = \gamma(t)/\gamma_0$ and (c) mean cluster size $\bar{M}(t) = M(t)/M_0$ for different values of Pe. Ring type ratio: 30:70. (b) Temporal evolution of the rescaled segregation parameter $\bar{\gamma}(t)$ and (d) mean cluster size $\bar{M}(t)$ for different ratios of ring types. The activity level is $Pe = 0.4$. The number of rings and the tension in all cases is $N = 10^4$ and $\Lambda = 10$, respectively.

By employing this comprehensive cellular model and incorporating a term for differential contraction among rings of different types, we conducted a numerical evaluation of Harris' proposed hypothesis on cellular differential surface contraction [6]. We observed a monotonic relationship between the differential contraction parameter Λ and the steady-state segregation parameter $\langle\gamma\rangle_t$, showing a tendency toward segregation for $\Lambda > 1$ and a checkerboard pattern for $\Lambda < 1$. We found that by keeping all cells with identical attraction forces and solely employing adequate differential interfacial contraction the system segregates. The differences in ring areas are minimal, which rules this out as a potential segregation mechanism [38]. (See Supplementary Material [32]). Mechanisms such as motility-induced phase separation (MIPS) are also dismissed since the Péclet values used here ($Pe \leq 0.7$) are well below the range where this transition occurs [39–41].

The rate at which the system transitions from an initially mixed state to its asymptotic state, as well as the ultimate value it reaches, also depends on the activity level Pe. In the case of segregation ($\Lambda > 1$), increased activity has a tendency to disrupt the configuration of minimum interfacial energy. Binodal curves, showing a transition between the mixed and the segregated states, corroborate the inverse correlation between the contraction interaction Λ and the activity Pe. These findings suggest that the activity Pe plays a role similar to temperature

in thermodynamic equilibrium systems [30, 31, 42].

Furthermore, we found that the segregation parameter $\gamma(t)$ and the mean cluster size $M(t)$ exhibit a power-law regime with an exponent close to $-1/3$ and $2/3$, respectively. The activity Pe changes the typical timescale at which the asymptotic regime begins but does not modify the growth exponent of the domains. Similarly, the proportions do not alter the characteristic exponent, except in the (50:50) case where the system starts close to percolation and the evolution appears to be dominated by rounding. We observed an inverse relationship between the segregation parameter and the typical size, $\gamma \sim M^{-2}$.

Finally, the observed segregation exponent of $\lambda = -1/3$ is at odds with the literature. The cluster-cluster aggregation mechanism seen in our simulations would typically correspond to an exponent of $\lambda = -1/4$, as predicted by surface diffusion models [43, 44] or mean cluster models [45, 46], particularly in the absence of alignment interactions. An exponent of $\lambda = -1/3$ would instead be expected from the Cahn-Hilliard equation if the mechanism were evaporation-condensation, which we do not observe. The reasons for these discrepancies will be explored in future studies.

We express our gratitude to the Brazilian agencies CAPES, CNPq, and FAPERGS for their financial support. H.C.M.F. and L.G.B. acknowledge the support from the National Council for Scientific and Technological Development – CNPq (procs. 402487/2023-0 and 443517/2023-1). E.F.T. acknowledges ICTP-SAIFR/IFT-UNESP. The simulations were conducted using the VD Lab cluster infrastructure at IF-UFRGS. This work is dedicated to the memory of Albert Kenneth Harris Jr.

* emanuel.teixeira@ufrgs.br
† carine@if.ufrgs.br
‡ heitor.fernandes@ufrgs.br
§ leon@if.ufrgs.br

[1] R. G. Harrison, Journal of Experimental Zoology **9**, 787 (1910).
[2] A. Moscona, Experimental Cell Research **3**, 535 (1952).
[3] J. P. Trinkaus and P. W. Groves, Proceedings of the National Academy of Sciences **41**, 787 (1955).
[4] P. Weiss and A. Taylor, Proceedings of the National Academy of Sciences **46**, 1177 (1960).
[5] M. S. Steinberg, Science **141**, 401 (1963).
[6] A. K. Harris, Journal of Theoretical Biology **61**, 267 (1976).
[7] G. W. Brodland, J. Biomech. Eng. **124**, 188 (2002).
[8] F. Graner and J. A. Glazier, Physical review letters **69**, 2013 (1992).
[9] J. Käfer, T. Hayashi, A. F. Marée, R. W. Carthew, and F. Graner, Proceedings of the National Academy of Sciences **104**, 18549 (2007).
[10] M. Krieg, Y. Arboleda-Estudillo, P.-H. Puech, J. Käfer, F. Graner, D. Müller, and C.-P. Heisenberg, Nature cell biology **10**, 429 (2008).
[11] A. Nakajima and S. Ishihara, New Journal of Physics **13**, 033035 (2011).
[12] L. Canty, E. Zarour, L. Kashkooli, P. François, and F. Fagotto, Nature communications **8**, 157 (2017).
[13] M. Durand, PLOS Computational Biology **17**, e1008576 (2021).
[14] D. L. Barton, S. Henkes, C. J. Weijer, and R. Sknepnek, PLOS Computational Biology **13**, 1 (2017).
[15] D. M. Sussman, J. Schwarz, M. C. Marchetti, and M. L. Manning, Physical review letters **120**, 058001 (2018).
[16] H. B. Wolff, L. A. Davidson, and R. M. Merks, Bulletin of Mathematical Biology **81**, 3322 (2019).
[17] M. Krajnc, Soft Matter **16**, 3209 (2020).
[18] J. C. M. Mombach, J. A. Glazier, R. C. Raphael, and M. Zajac, Phys. Rev. Lett. **75**, 2244 (1995).
[19] M. L. Manning, R. A. Foty, M. S. Steinberg, and E.-M. Schoetz, Proc Natl Acad Sci U S A **107**, 12517 (2010).
[20] A. Boromand, A. Signoriello, F. Ye, C. S. O'Hern, and M. D. Shattuck, Physical Review Letters **121**, 248003 (2018).
[21] J. D. Treado, D. Wang, A. Boromand, M. P. Murrell, M. D. Shattuck, and C. S. O'Hern, Physical Review Materials **5**, 055605 (2021).
[22] E. F. Teixeira, H. C. Fernandes, and L. G. Brunnet, Soft Matter **17**, 5991 (2021).
[23] G. Ourique, E. Teixeira, and L. Brunnet, Physica A: Statistical Mechanics and its Applications **589**, 126661 (2022).
[24] D. Bi, J. Lopez, J. M. Schwarz, and M. L. Manning, Nature Physics **11**, 1074 (2015).
[25] D. Bi, X. Yang, M. C. Marchetti, and M. L. Manning, Physical Review X **6**, 021011 (2016).
[26] B. Bhattacherjee, M. Hayakawa, and T. Shibata, Soft Matter **20**, 2739 (2024).
[27] T. Hiraiwa, Phys. Rev. Lett. **125**, 268104 (2020).
[28] J. LaChance, K. Suh, J. Clausen, and D. J. Cohen, PLoS computational biology **18**, e1009293 (2022).
[29] H. Yamanaka and S. Kondo, Proceedings of the National Academy of Sciences **111**, 1867 (2014).
[30] Y. Fily and M. C. Marchetti, Physical review letters **108**, 235702 (2012).
[31] Y. Fily, S. Henkes, and M. C. Marchetti, Soft matter **10**, 2132 (2014).
[32] See Supplemental Material at [URL will be inserted by publisher] for videos and simulation details, which includes Refs. [14, 17, 20, 24, 25, 38].
[33] J. M. Belmonte, G. L. Thomas, L. G. Brunnet, R. M. C. de Almeida, and H. Chaté, Phys. Rev. Lett. **100**, 248702 (2008).
[34] C. P. Beatrici, R. M. C. de Almeida, and L. G. Brunnet, Phys. Rev. E **95**, 032402 (2017).
[35] F. Franke, S. Aland, H.-J. Böhme, A. Voss-Böhme, and S. Lange, PLoS computational biology **18**, e1010460 (2022).
[36] S. N. Weber, C. A. Weber, and E. Frey, Physical review letters **116**, 058301 (2016).
[37] J.-P. Rieu and Y. Sawada, The European Physical Journal B - Condensed Matter and Complex Systems **27**, 167 (2002).
[38] X. Yang, M. L. Manning, and M. C. Marchetti, Soft matter **10**, 6477 (2014).
[39] Y. Fily and M. C. Marchetti, Phys. Rev. Lett. **108**, 235702 (2012).

[40] G. S. Redner, M. F. Hagan, and A. Baskaran, Biophysical Journal **104**, 640a (2013).
[41] M. E. Cates and J. Tailleur, Annu. Rev. Condens. Matter Phys. **6**, 219 (2015).
[42] C. Bechinger, R. Di Leonardo, H. Löwen, C. Reichhardt, G. Volpe, and G. Volpe, Reviews of modern physics **88**, 045006 (2016).
[43] A. Sicilia, Y. Sarrazin, J. J. Arenzon, A. J. Bray, and L. F. Cugliandolo, Phys. Rev. E **80**, 031121 (2009).
[44] J. W. Cahn and J. E. Hilliard, The Journal of chemical physics **28**, 258 (1958).
[45] C. P. Beatrici, R. M. de Almeida, and L. G. Brunnet, Physical Review E **95**, 032402 (2017).
[46] M. Kolb, Phys. Rev. Lett. **53**, 1653 (1984).

Supplementary Material: Segregation in binary mixture with differential contraction among active rings

Emanuel F. Teixeira,* Carine P. Beatrici,† Heitor C. M. Fernandes,‡ and Leonardo G. Brunnet§
Instituto de Física, Universidade Federal do Rio Grande do Sul,
CP 15051, CEP 91501-970 Porto Alegre - RS, Brazil

A - BOUNDARY CONDITIONS - REPULSIVE CIRCULAR WALLS

We configure the system as a binary mixture of N active rings confined within a circular arena of radius R_0. The force exerted by the wall on a specific particle within a ring is given by

$$\vec{F}_w = -F_w \left(\frac{|\vec{r}_{i,j} - \vec{r}_{cm}|}{R_0} - 1 \right) \frac{(\vec{r}_{i,j} - \vec{r}_{cm})}{|\vec{r}_{i,j} - \vec{r}_{cm}|} \tag{1}$$

where $\frac{(\vec{r}i,j-\vec{r}cm)}{|\vec{r}i,j-\vec{r}cm|}$ is the unit vector connecting the center of particle i within ring j to the center of mass, and F_w is the characteristic force exerted by the wall on the particle.

B - FORCES

We derive the analytical expressions for the forces acting on each particle i within a ring j. These particles are subjected to forces resulting from both shape and interaction energies, which are determined by the area, perimeter, differential line tension, particle-particle overlap, and adhesion terms as defined in the main text. The force on particle i in ring j is obtained by taking the vector derivative of the total energy E with respect to its coordinates.

$$\vec{r}_{i,j} = x_{i,j}\hat{e}_x + y_{i,j}\hat{e}_y, \tag{2}$$

$$\vec{F}_{i,j} = -\frac{\partial E}{\partial \vec{r}_{i,j}} \equiv -\frac{\partial E}{\partial x_{i,j}}\hat{e}_x - \frac{\partial E}{\partial y_{i,j}}\hat{e}_y. \tag{3}$$

Perimeter force

The perimeter energy, as defined in the main text for a configuration of N rings labeled by $j = 1, \ldots, N$, with n particles labeled $i = 1, \ldots, n$, is given by

$$E_P = \frac{\epsilon_P}{2} \sum_{j=1}^{N} \sum_{i=1}^{n} \left(\frac{|\vec{l}_{i,j}|}{l_0} - 1 \right)^2. \tag{4}$$

The force on particle i due to deviations in the segment length $|\vec{l}_{i,j}| = |\vec{r}_{i,j} - \vec{r}_{i-1,j}|$ from its preferred value l_0 is given by

$$\vec{F}_P^{i,j} = -\frac{\partial E_P}{\partial \vec{r}_{i,j}} = -\frac{\partial E_P}{\partial x_{i,j}}\hat{e}_x - \frac{\partial E_P}{\partial y_{i,j}}\hat{e}_y, \tag{5}$$

$$\vec{F}_P^{i,j} = -\frac{\epsilon_P}{l_0} \left[\left(\frac{|\vec{l}_{i,j}|}{l_0} - 1 \right) \frac{\partial |\vec{l}_{i,j}|}{\partial \vec{r}_{i,j}} - \left(\frac{|\vec{l}_{i+1,j}|}{l_0} - 1 \right) \frac{\partial |\vec{l}_{i+1,j}|}{\partial \vec{r}_{i+1,j}} \right], \tag{6}$$

$$\vec{F}_P^{i,j} = \frac{\epsilon_P}{l_0} \left[\left(\frac{|\vec{l}_{i+1,j}|}{l_0} - 1 \right) \frac{\vec{l}_{i+1,j}}{|\vec{l}_{i+1,j}|} - \left(\frac{|\vec{l}_{i,j}|}{l_0} - 1 \right) \frac{\vec{l}_{i,j}}{|\vec{l}_{i,j}|} \right], \tag{7}$$

where we use the following relations:

$$\frac{\partial|\vec{l}_{i,j}|}{\partial\vec{r}_{i,j}} = \frac{\partial|\vec{l}_{i,j}|}{\partial x_{i,j}}\hat{e}_x + \frac{\partial|\vec{l}_{i,j}|}{\partial y_{i,j}}\hat{e}_y = -\frac{\vec{l}_{i,j}}{|\vec{l}_{i,j}|}, \tag{8}$$

$$\frac{\partial|\vec{l}_{i+1,j}|}{\partial\vec{r}_{i+1,j}} = \frac{\partial|\vec{l}_{i+1,j}|}{\partial x_{i+1,j}}\hat{e}_x + \frac{\partial|\vec{l}_{i+1,j}|}{\partial y_{i+1,j}}\hat{e}_y = \frac{\vec{l}_{i+1,j}}{|\vec{l}_{i+1,j}|}. \tag{9}$$

Area force

The force related to area energy on particle i in ring j is given by

$$\vec{F}_A^{i,j} = -\frac{\partial E_A}{\partial\vec{r}_{i,j}} = -\frac{\epsilon_A}{A_0}\left(\frac{A_j}{A_0} - 1\right)\frac{\partial A_j}{\partial\vec{r}_{i,j}}, \tag{10}$$

being E_A the area energy defined by

$$E_A = \frac{\epsilon_A}{2}\sum_{j=1}^{N}\left(\frac{A_j}{A_0} - 1\right)^2. \tag{11}$$

The ring area A_j is calculated using the vector product property, given by

$$A_j = \frac{1}{2}\sum_{j}^{n}|(\vec{r}_{i,j} - \vec{r}_{cm}) \times \vec{l}_{i,j}| = \frac{1}{2}\sum_{j}^{n}(x_{i,j} - x_{cm})(y_{i,j} - y_{i-1,j}) - (y_{i,j} - y_{cm})(x_{i,j} - x_{i-1,j}), \tag{12}$$

where the factor $1/2$ is included to avoid double-counting the area. Therefore, we obtain:

$$\frac{\partial A_j}{\partial x_{i,j}} = \frac{(y_{i+1,j} - y_{i-1,j})}{2}, \tag{13}$$

$$\frac{\partial A_j}{\partial y_{i,j}} = \frac{(x_{i+1,j} - x_{i-1,j})}{2}, \tag{14}$$

thus,

$$\vec{F}_A^{i,j} = -\frac{\partial E_A}{\partial\vec{r}_{i,j}} = -\frac{\epsilon_A}{2A_0}\left(\frac{A_j}{A_0} - 1\right)\left[(y_{i+1,j} - y_{i-1,j})\,\hat{e}_x - (x_{i+1,j} - x_{i-1,j})\,\hat{e}_y\right]. \tag{15}$$

Interaction forces

The core repulsion for non-neighboring particles within the same ring and the adhesion between particles of different rings are accounted for by the interaction energy E_{int}, which is described by a truncated harmonic potential,

$$E_{int} = \begin{cases} \frac{\epsilon_c}{2}\left(\frac{r_{ik}}{\sigma} - 1\right)^2, & r_{ik} \le \sigma \\ \frac{\epsilon_{adh}}{2}\left(\frac{r_{ik}}{\sigma} - 1\right)^2, & l_{adh} \ge r_{ik} > \sigma \\ 0, & r_{ik} > l_{adh}. \end{cases} \tag{16}$$

Therefore, the corresponding force

$$\vec{F}_{int}^{i,j} = -\frac{\partial E_{int}}{\partial \vec{r}_{i,j}}, \tag{17}$$

$$\vec{F}_{int}^{i,j} = \hat{r}_{ik} \begin{cases} -\frac{\epsilon_c}{\sigma}\left(\frac{r_{ik}}{\sigma} - 1\right), & r_{ik} \leq \sigma \\ -\frac{\epsilon_{adh}}{\sigma}\left(\frac{r_{ik}}{\sigma} - 1\right), & l_{adh} \geq r_{ik} > \sigma \\ 0, & r_{ik} > l_{adh} \end{cases} \tag{18}$$

where $\hat{r}_{ik} = \frac{\vec{r}_{ik}}{r_{ik}}$ is a unit vector connecting particle i and k.

Differential line tension (contraction)

The contraction energy represents a line tension that acts between two particles from different rings when they are within a distance cutoff l_Λ. This energy term is given by

$$E_\Lambda = \sum_{j=1}^{N}\sum_{i=1}^{n} \Lambda_{\alpha\beta}|\vec{l}_{i,j}|. \tag{19}$$

The force acting on particle i inside ring j is

$$\vec{F}_\Lambda^{i,j} = -\frac{\partial E_\Lambda}{\partial \vec{r}_{i,j}}, \tag{20}$$

$$\vec{F}_\Lambda^{i,j} = \Lambda_{\alpha\beta}\left[\frac{\vec{l}_{i+1,j}}{|\vec{l}_{i+1,j}|} - \frac{\vec{l}_{i,j}}{|\vec{l}_{i,j}|}\right]. \tag{21}$$

Therefore, the force $\vec{F}_\Lambda^{i,j}$ on particle i within ring j depends on the type α of its ring and the type β of the ring of the particle it interacts with. If the particle is within the cutoff distance and interacts with multiple particles from other rings, the tension value will be the mean of all the individual tensions. Specifically, this mean is given by

$$\Lambda_{\alpha\beta} = \frac{1}{n_c}\sum_k \Lambda_{\alpha k}, \tag{22}$$

where the sum k runs over all contacts (both $\alpha - \alpha$ and $\alpha - \beta$ interactions) and n_c represents the total number of contacts.

C - CONTROL PARAMETERS

The value of the total equilibrium area A_r is the sum of the equilibrium area imposed by the area elastic energy term plus half the area of each particle composing the ring,

$$A_r = A_0 + \frac{n\pi\sigma^2}{8}. \tag{23}$$

We define a packing fraction ϕ for the system, relative to a circular region of radius R_0, through the relation

$$\phi = \frac{NA_r}{\pi R_0^2}. \tag{24}$$

We fix $\phi = 0.895$ allowing for neighbor exchange and neighbor interaction simultaneously and we use a fixed dimensionless perimeter-area equilibrium ratio $p_0 = P_0/\sqrt{A_0} = 4$, where $P_0 = nl_0$ is the equilibrium perimeter. The shape parameter p_0 defines the degree of stiffness of the ring. The choice of this value is based on previous works with Vertex [1–3], Voronoi [4], and ring models [5], where an excess of cell perimeter is found for $p_0 > 3.81$ as well as the

emergence of a liquid-like behavior. To prevent overlap among rings, we reached a compromise by setting comparable values for ϵ_c, ϵ_P and ϵ_A, while assigning a much lower value to ϵ_{adh}. So, we simulate the ring system keeping the following parameters fixed: $\epsilon_P = 20$, $\epsilon_c/\epsilon_P = 1$, $\epsilon_A/\epsilon_P = 35$, $(F_w\sigma)/\epsilon_P = 1$, $\epsilon_{adh}/\epsilon_P = 5.10^{-4}$, $n = 10$, $l_0 = 1$, $\tau_R = 1$, $\sigma = l_0$, $l_\Lambda = l_{adh} = 1.5\,l_0$ and $\mu = 1$. Using the previous definitions and the range $(0.1 < Pe < 0.7)$, the interval for v_0 is determined to be $[0.1, 0.7]$. Copy The mechanical moduli then are $K_P = \frac{\epsilon_P}{l_0^2} = 20$ and $K_A = \frac{\epsilon_A}{A_0^2} = 17.92$. This choice of parameters ensures that ϵ_P and ϵ_A are sufficiently large to maintain the bond length close to l_0 and the equilibrium area close to A_0. The adhesion forces between different rings are kept equal for all rings. Furthermore, to emphasize the effects of differential contractions, we adopted an adhesion value that is considerably lower compared to the other energy terms involved. We integrate the equations of motion, using the Euler-Maruyama algorithm with a time step $\Delta t = 0.01$.

D - Neighbors criterion for measurements

In this work, we use the criterion for defining whether two rings are neighbors based on the distance between their centers of mass, $d_{jk} = |\vec{R}_j - \vec{R}_k| \leq \frac{P_0}{2} = 5\sigma$. This relation ensures that even two completely flattened rings in contact will be considered neighbors.

E - Phase diagram $\Lambda_{12} \times (\Lambda_{11} - \Lambda_{22})$

We examined the diagram $\Lambda_{12} \times (\Lambda_{11} - \Lambda_{22})$ with $\Lambda_{11} = 1$ to specifically assess the impact of differential contraction $(\Lambda_{12} > 0)$ apart from other potential influences on the segregation process. We varied Λ_{22} within the range [5:0] and noted that when $\Lambda_{12} = 0$, segregation does not occur due to any underlying mechanisms. Conversely, we observed a checkerboard-like pattern, where higher values of Λ_{22} lead to a preference for different types of rings while avoiding rings of the same type.

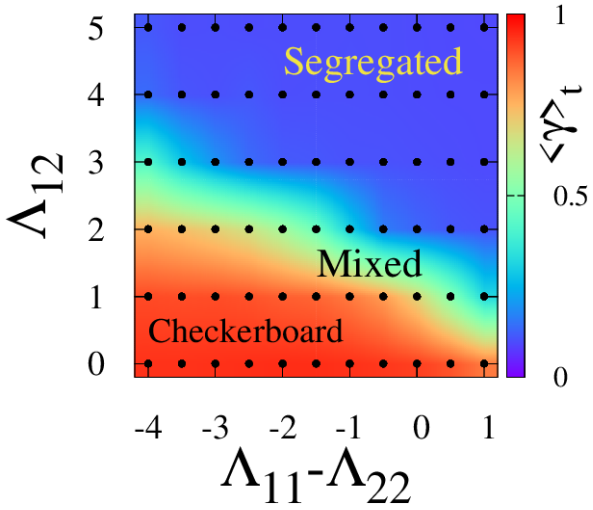

FIG. 1. Phase diagram $\Lambda_{12} \times (\Lambda_{11} - \Lambda_{22})$ that separates checkerboard, mixed and segregated regions. Colors represent the average values of segregation parameter for long times. Fixed parameters: $N = 500$, $Pe = 0.4$ and $\phi = 0.9$.

F -Maximum variation in the areas of the rings due to contraction

The contraction term introduced in this work tends to effectively reduce the size of the ring when it interacts with another ring. Since difference in particle size may also induce segregation [6], we will analyze here the maximum variation due to contraction. Throughout this study, the maximum value of differential contraction is $\Lambda_{12} = 5$. The contraction terms are kept constant at $\Lambda_{11} = \Lambda_{22} = 0.5$. Perimeter (spring) forces and area forces act to maintain

the initial configuration, while the contraction term drives changes. Thus, at equilibrium, the following relationship is satisfied:

$$k_P \delta l - \Lambda_{12} + k_A \delta A = 0, \tag{25}$$

where δl is a variation in the distances between particles on the membrane, and δA is the variation in the area. The area of a regular polygon is given by

$$A = \frac{n l^2}{4 \tan\left(\frac{\pi}{n}\right)}. \tag{26}$$

The variation of area around equilibrium is given by

$$\delta A|_{l=l_0} = \frac{n l_0 \delta l}{2 tan(\frac{\pi}{n})}. \tag{27}$$

Using Eq. 27 in Eq. 25, we obtain

$$\delta l = \frac{\Lambda_{12}}{k_P + \frac{k_A n l_0}{2 \tan\left(\frac{\pi}{n}\right)}}. \tag{28}$$

Thus, the relative variation of the area around equilibrium is given by

$$\left.\frac{\delta A}{A}\right|_{l=l_0} = \frac{2\delta l}{l_0}. \tag{29}$$

Thus, by substituting Eq. 28 into Eq. 29, we obtain

$$\left.\frac{\delta A}{A}\right|_{l=l_0} = \frac{2}{l_0} \frac{\Lambda_{12}}{k_P + \frac{k_A n l_0}{2 \tan\left(\frac{\pi}{n}\right)}} \sim 0.017, \tag{30}$$

where we use $k_P = 20$, $k_A = 17.92$, $l_0 = 1$, $n = 10$ and $\Lambda_{12} = 5$. We demonstrate that the difference in ring sizes is less than 2%, while the literature [6] indicates that particles of one type should be twice the size of the others for segregation induced by size differences to take place.

VIDEOS CAPTIONS

- Video 1: Simulation of a binary mixture of rings with differential membrane contraction. Time is in log scale. Set parameters: $N = 1000$, $Pe = 0.3$, $\Lambda = 0.1$ and Ring type ratio: (30:70). → Fig 2a
- Video 2: Simulation of a binary mixture of rings with differential membrane contraction. Time is in log scale. Set parameters: $N = 1000$, $Pe = 0.3$, $\Lambda = 1.5$ and Ring type ratio: (30:70). → Fig 2a
- Video 3: Simulation of a binary mixture of rings with differential membrane contraction. Time is in log scale. Set parameters: $N = 1000$, $Pe = 0.3$, $\Lambda = 10$ and Ring type ratio: (30:70). → Fig 2a
- Video 4: Simulation of a binary mixture of rings with differential membrane contraction. Time is in log scale. Set parameters: $N = 10000$, $Pe = 0.4$, $\Lambda = 10$ and Ring type ratio: (10:90). → Fig 4c-d
- Video 5: Simulation of a binary mixture of rings with differential membrane contraction. Time is in log scale. Set parameters: $N = 10000$, $Pe = 0.4$, $\Lambda = 10$ and Ring type ratio: (30:70). → Fig 4
- Video 6: Simulation of a binary mixture of rings with differential membrane contraction. Time is in log scale. Set parameters: $N = 10000$, $Pe = 0.4$, $\Lambda = 10$ and Ring type ratio: (50:50). → Fig 4c-d

* emanuel.teixeira@ufrgs.br

† carine@if.ufrgs.br
‡ heitor.fernandes@ufrgs.br
§ leon@if.ufrgs.br

[1] D. Bi, J. Lopez, J. M. Schwarz, and M. L. Manning, Nature Physics **11**, 1074 (2015).
[2] D. L. Barton, S. Henkes, C. J. Weijer, and R. Sknepnek, PLOS Computational Biology **13**, 1 (2017).
[3] M. Krajnc, Soft Matter **16**, 3209 (2020).
[4] D. Bi, X. Yang, M. C. Marchetti, and M. L. Manning, Physical Review X **6**, 021011 (2016).
[5] A. Boromand, A. Signoriello, F. Ye, C. S. O'Hern, and M. D. Shattuck, Physical Review Letters **121**, 248003 (2018).
[6] X. Yang, M. L. Manning, and M. C. Marchetti, Soft matter **10**, 6477 (2014).

Part II

Aggregation Kinetics in Active Matter

Chapter 3

Cluster Aggregation

The first part of this thesis investigated the physical hypotheses underlying cell segregation, a fundamental process driving tissue and organ formation during embryogenesis and morphogenesis. Particular emphasis was placed on the Differential Surface Contraction Hypothesis (DSCH), originally proposed by Harris. To test this hypothesis in isolation, we developed a computational model based on deformable active membranes with localized contractile interactions.

The results, detailed in the corresponding publication [64], demonstrated that cell segregation proceeds as an aggregation process, where clusters progressively coalesce into larger domains. These domains evolve in time, and the typical cluster size, quantified by the average cluster mass, follows an algebraic growth law of the form $\overline{M}(t) \sim t^z$. In our simulations, we observed scaling exponents in the range $1/2 < z < 2/3$, with typical values approaching $z \approx 2/3$. Although this exponent is often associated with the so-called Ostwald ripening mechanism [24], where smaller clusters dissolve and their material condenses onto larger ones, such behavior was not observed in our system. Instead, the coarsening dynamics were found to be driven by the physical coalescence of entire clusters.

In the second part of this thesis, we shift focus toward a more detailed understanding of the kinetics of aggregation during tissue formation, examining how collective motion and persistence of the clusters influence the temporal evolution of cluster growth in active cellular systems.

3.1 Mechanisms of Cluster Growth

The process of demixing, where an initially mixed system evolves into well separated domains is fundamentally governed by the kinetics of domain growth. Two idealized pathways are typically considered: (i) an evaporation–condensation process, or (ii) the aggregation and coalescence of clusters (see Fig. 3.1). In realistic systems, both mechanisms may coexist or compete, depending on material properties and environmental conditions.

The dynamics of these processes are generally determined by the interplay between two competing tendencies: the rate at which clusters grow, and the relaxation of their interfaces toward minimal surface energy configurations. In the evaporation–condensation mechanism, individual units detach from smaller clusters and attach to larger, more stable ones. A defining feature of this mechanism is that the centers of mass of the clusters remain fixed in space, while material is exchanged between them (see Fig. 3.1).

A classical example of this behavior is Ostwald ripening process, in which domain

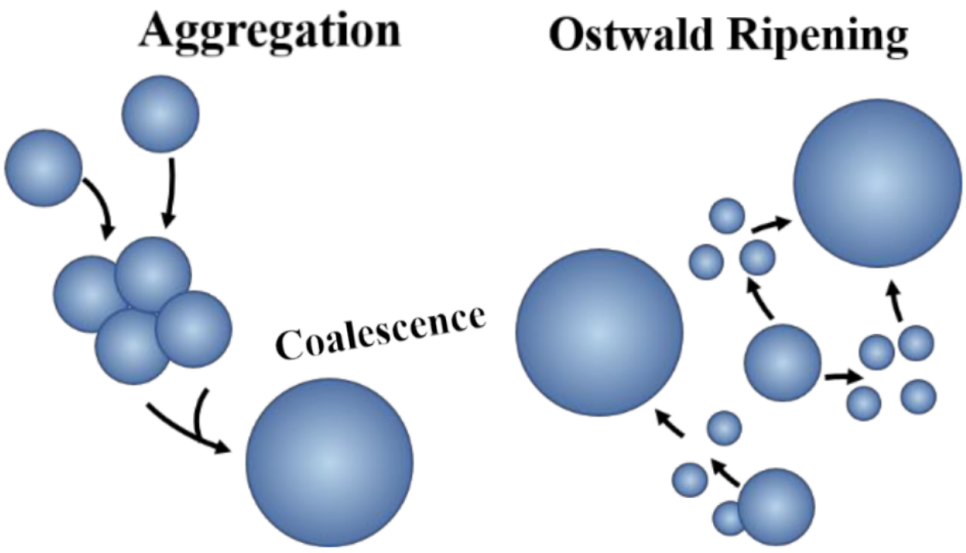

Figure 3.1: Schematic comparison between two idealized mechanisms of domain growth during demixing. In the evaporation–condensation (or Ostwald ripening) process, small clusters shrink while larger clusters grow by exchange of individual units through the medium, with fixed cluster positions. This leads to slow mass transfer controlled by diffusion. In contrast, the aggregation mechanism involves the physical motion and merging of entire clusters, conserving their mass.

growth is limited by the diffusive transport of material from smaller to larger clusters. This regime is described by the Lifshitz–Slyozov–Wagner (LSW) theory [22–24], which predicts a power-law growth of the typical domain size $R(t) \sim t^{\lambda}$, with a universal exponent $\lambda = 1/3$, independent of spatial dimension. Since the average cluster mass scales as $\overline{M} \sim R^d$, the corresponding mass growth exponent becomes $z = d\lambda$. In two dimensions, this yields $z = 2/3$.

3.2 The Smoluchowski Coagulation Equation

In biological cell systems, such as during cell segregation, cells may adhere both to one another and to the surrounding substrate. Once formed, cellular clusters tend to be mechanically stable and may exhibit coordinated internal motion due to collective dynamics. As a result, domain growth in these systems is often governed by a kinetic pathway of cluster aggregation [2, 3, 5]. This mechanism involves the physical movement and merging of entire clusters. For aggregation to occur, clusters must be mobile, moving through the medium until they encounter one another and fuse into larger structures. In this regime, the coarsening dynamics are governed primarily by the translational motion of clusters as composite units, rather than by the exchange of individual cells between domains.

The general theoretical framework for describing cluster aggregation is provided by the Smoluchowski coagulation equation [69]. This approach considers a population of clusters of varying masses moving through space. When two clusters of masses M and M' come into contact, they may merge into a new cluster of mass $M + M'$, via the reaction:

$$A_M + A_{M'} \xrightarrow[K(M,M')]{} A_{M+M'}, \tag{3.1}$$

where A_M denotes a cluster of mass M, and $K(M, M')$ is the coagulation kernel that

defines the rate at which two clusters of masses M and M' merge.

The Smoluchowski theory adopts a mean-field approximation with spatial homogeneity, assuming that the cluster mass distribution is uniform across the system $P(\mathbf{r}, M, t) = P(M, t)$. The total number of clusters of mass M in a d-dimensional hypercubic volume $V_0 = L^d$ is described by the mass distribution $P(M, t)$, defined by:

$$\int_{V_0} P(\mathbf{r}, M, t)\, dV = P(M, t)\, V_0. \tag{3.2}$$

The mass distribution concentration of clusters of mass M is then given by:

$$C(M, t) = \frac{P(M, t)}{V_0}. \tag{3.3}$$

The concentration $C(M, t)$ increases when two smaller clusters of masses M' and $M - M'$ merge to form a cluster of mass M. The rate of this process is proportional to the product $C(M', t)\, C(M - M', t)$. On the other hand, when a cluster of mass M merges with any other cluster, it is removed from the population, resulting in a decrease in $C(M, t)$. To describe the full aggregation process, we integrate over the coagulating masses, treated as continuous variables:

$$\begin{aligned}\frac{\partial C(M, t)}{\partial t} = \frac{1}{2}\int_0^M K(M', M - M')\, C(M', t)\, C(M - M', t)\, dM' \\ - \int_0^\infty K(M, M')\, C(M, t)\, C(M', t)\, dM',\end{aligned} \tag{3.4}$$

where $K(M, M')$ is the coagulation kernel. The prefactor $1/2$ ensures that the contribution is not double-counted. Equation (3.4) represents the Smoluchowski coagulation equation [69] in its continuous form. In terms of the mass distribution $P(M, t)$, Eq. (3.4) becomes

$$\begin{aligned}\frac{\partial P(M, t)}{\partial t} = \frac{1}{2V_0}\int_0^M K(M', M - M')\, P(M', t)\, P(M - M', t)\, dM' \\ - \frac{1}{V_0}\int_0^\infty K(M, M')\, P(M, t)\, P(M', t)\, dM'.\end{aligned} \tag{3.5}$$

This is the Smoluchowski coagulation equation for the cluster mass distribution. The coagulation kernel $K(M, M')$ encapsulates the physical properties related to cluster interactions and mobility, and it plays a central role in determining the scaling laws and kinetic regimes of the aggregation process.

An important feature of this framework is that the total mass is conserved, which can be expressed as:

$$M_0 = \int_0^\infty M\, P(M, t)\, dM = \text{const}. \tag{3.6}$$

The average cluster mass is defined by:

$$\overline{M}(t) = \frac{\int_0^\infty M\, P(M, t)\, dM}{\int_0^\infty P(M, t)\, dM}, \tag{3.7}$$

and its time evolution can be obtained from Eq. (3.5) (see Supplementary Material of Article 2), yielding:

$$\frac{d\overline{M}(t)}{dt} = \frac{\overline{M}(t)^2}{2\, M_0\, V_0}\int_0^\infty \int_0^\infty K(M, M')\, P(M, t)\, P(M', t)\, dM'\, dM. \tag{3.8}$$

In general, Eqs. (3.5) and (3.8) cannot be solved analytically, and only a few specific forms of the coagulation kernel $K(M, M')$ admit exact analytical solutions. Exact analytical solutions to the Smoluchowski coagulation equation are known only for a few specific classes of kernels [25, 28, 70]. The most well-established among them are: the constant kernel $K(x, y) = A$, the additive kernel $K(x, y) = A(x + y)$, and the multiplicative kernel $K(x, y) = C\,x\,y$.

3.2.1 Diffusion-Limited Cluster Aggregation (DLCA)

When the typical timescale for collisions between clusters is longer than the time required for a cluster to diffuse across its own size, the aggregation process enters the diffusion-limited regime, known as Diffusion-Limited Cluster Aggregation (DLCA). Consider a spherical object of radius R surrounded by Brownian particles with diffusion coefficient D. The absorption rate of particles by the sphere scales as $K \sim DR^{d-2}$ [25, 28]. Extending this result to aggregating clusters, where both entities are mobile, leads to the expression for the Brownian kernel [25–28]:

$$\begin{aligned} K(M, M') &= A\,[D(M) + D(M')]\,[R(M) + R(M')]^{d-2} \\ &= A\,(M^{\alpha} + M'^{\alpha})\left(M^{1/d_f} + M'^{1/d_f}\right)^{d-2}, \end{aligned} \tag{3.9}$$

where:

- A is a constant with units to guarantee dimensional consistency;
- $R(M) \sim M^{1/d_f}$ is the radius of gyration of a cluster with mass M, characterized by the fractal dimension d_f;
- $D(M) \sim M^{\alpha}$ describes the scaling of the diffusion coefficient with cluster mass.

Unlike the classical scenario of static absorbers in a sea of diffusing particles, in DLCA the clusters themselves are mobile and merge upon encounter. Consequently, the coagulation kernel accounts for the combined contributions of both cluster mobilities and sizes. Substituting Eq. (3.9) into the growth law for the average cluster mass, Eq. (3.8), the Smoluchowski framework predicts (see supplementary material) a power-law behavior:

$$\overline{M}(t) \sim t^{z}, \tag{3.10}$$

with the dynamic exponent given by:

$$z = \frac{d_f}{d_f - d_f\alpha - (d-2)}. \tag{3.11}$$

In two dimensions ($d = 2$), this expression simplifies to:

$$z = \frac{1}{1-\alpha}. \tag{3.12}$$

For a cluster formed by particles with uncorrelated velocities, the diffusion coefficient scales as $D(M) \sim M^{-1}$, corresponding to $\alpha = -1$ [31, 71]. In this case, the expected dynamic exponent is $z = 1/2$, consistent with classical diffusion. In contrast, for clusters formed by particles with aligned and strongly correlated velocities, such as in systems with collective motion—the diffusion coefficient becomes independent of mass, $D(M) \sim$ const, i.e., $\alpha = 0$. This leads to a faster coarsening regime with a scaling exponent $z = 1$.

3.2.2 Ballistic Aggregation

In systems where clusters move in highly persistent, straight-line trajectories, the aggregation process enters the ballistic regime. Here, collisions are dominated by the clusters' relative speeds and geometrical cross-sections, rather than by random diffusion. A widely used form of the coagulation kernel for ballistic aggregation is [25, 29]:

$$\begin{aligned} K(M, M') &= B\,|V(M) - V(M')|\,(R(M) + R(M'))^{d-1} \\ &= B\,|M^{\gamma} - M'^{\gamma}|\left(M^{1/d_f} + M'^{1/d_f}\right)^{d-1}, \end{aligned} \tag{3.13}$$

where:

- B is a constant with appropriate units to ensure dimensional consistency;
- $|V(M) - V(M')|$ represents the relative velocity between clusters;
- $R(M) \sim M^{1/d_f}$ is the cluster size, and d_f its fractal dimension;
- $V(M) \sim M^{\gamma}$ describes the scaling of cluster speed with mass.

The exponent γ reflects the internal alignment of constituent particles within clusters. For uncorrelated particles, the center-of-mass speed decreases with cluster size, typically as $\gamma = -1/2$. In contrast, for clusters exhibiting strong alignment and coherent motion, the speed becomes independent of mass, leading to $\gamma = 0$. As in the diffusive case, inserting Eq. (3.13) into the Smoluchowski framework yields an algebraic growth of the average cluster mass (see supplementary material):

$$\overline{M}(t) \sim t^{z}, \tag{3.14}$$

with the dynamic exponent now given by:

$$z = \frac{d_f}{d_f - d_f\gamma - (d-1)}. \tag{3.15}$$

In the limit of compact (non-fractal) clusters, where $d = d_f$, this expression reduces to:

$$z = \frac{d}{1 - d\gamma}. \tag{3.16}$$

For instance, in two dimensions:

- For uncorrelated velocities ($\gamma = -1/2$), one obtains $z = 1$;
- For fully correlated velocities ($\gamma = 0$), the coarsening becomes significantly faster, with $z = 2$.

These results highlight the crucial role of internal cluster dynamics and motion persistence in determining the speed and universality class of the aggregation process. The DLCA and ballistic regimes thus represent two fundamental limits of coarsening kinetics in systems of aggregation clusters.

3.3 Beyond Classical Coarsening: The Impact of Collective Cell Motion

Classical coarsening models, which describe cluster growth as a passive process driven by thermal fluctuations and interfacial tension, fail to account for the rapid domain formation observed in developing tissues. A growing body of evidence (see references below) indicates that active processes, particularly those emerging from collective cell motion are key drivers of accelerated tissue patterning and cell segregation. Several landmark studies have progressively shaped this revised perspective:

Velocity alignment as a driver of segregation: The seminal self-propelled particle model by Belmonte et al. [44] showed that local alignment of velocities among neighboring cells leads to coherent collective motion, which markedly enhances the rate of cluster coalescence and domain growth.

Collective migration: Méhes et al. [5] provided experimental evidence that stronger collective migration correlates with faster segregation. Their co-culture experiments revealed domain growth exponents as high as $z \approx 1.5$, far exceeding classical limits, including diffusion-limited growth ($z = 1/2$), Ostwald ripening ($z = 2/3$), and even ballistic aggregation ($z = 1$).

Differential persistence: More recently, Bothe et al. [72] demonstrated that differential persistence, where one cell type temporarily increases its directional memory following heterotypic contact, can independently drive cell sorting. Furthermore, when combined with differential adhesion, this mechanism leads to even faster segregation kinetics.

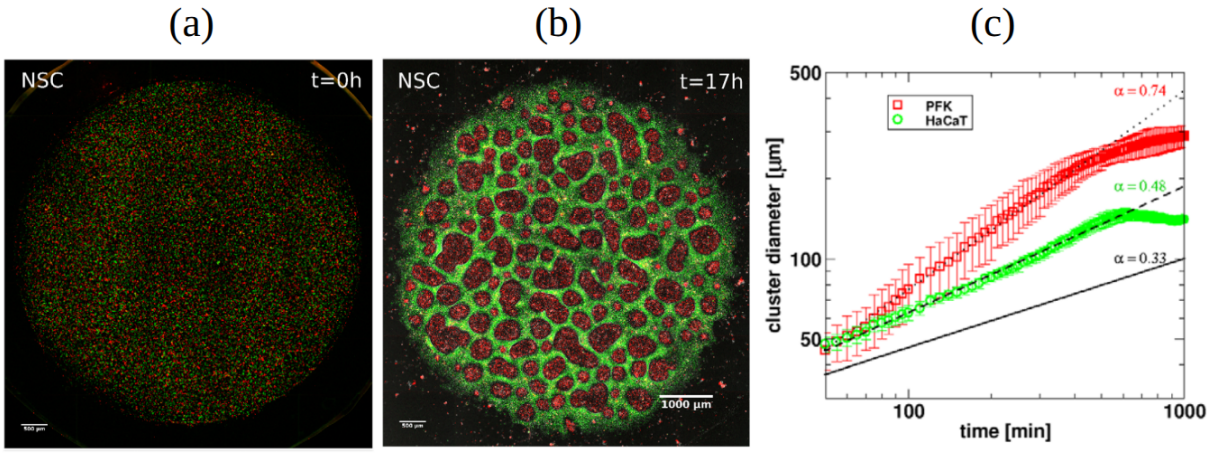

Figure 3.2: (a–b) Representative snapshots from co-culture experiments with motile keratocyte cell lines: primary goldfish keratocytes (red) and EPC fish keratocytes (green). The degree of segregation depends on the collective migration behavior of the two cell types. (c) Temporal evolution of the characteristic domain size, exhibiting algebraic growth $R(t) \sim t^{\lambda}$ with exponent $\lambda \approx 0.74$ for primary keratocytes (red curve) and $\lambda \approx 0.48$ for HaCaT keratinocytes (green curve). This corresponds to average cluster mass scaling $\overline{M}(t) \sim t^{z}$, with $z \approx 1.5$ and $z \approx 1$, respectively, in two dimensions. Adapted from Méhes *et al.* [5].

The transition to collective motion is traditionally understood as a consequence of spontaneous symmetry breaking, driven by alignment interactions among agents, as proposed by Vicsek *et al.* [8]. However, an alternative mechanism bypasses the need for

mutual alignment with neighbors. Proposed by Shimoyama *et al.* [73], this mechanism is based on **self-alignment**, where each particle adjusts its polarity to align with its own direction of motion. In this framework, the polarity, a vector defining the orientation of self-propulsion, is continuously reoriented by an **internal feedback** loop between the particle's motility and its orientation (see Fig. 3.3). This concept was successfully applied by Szabó *et al.* [19] to model the collective migration of keratocyte cells, demonstrating that self-alignment effectively captures *flocking* transitions in tissues.

Developing this idea, Mones *et al.* [30] proposed a minimal model of adhesive active disks, in which each particle's polarity gradually reorients toward its instantaneous velocity (see Fig. 3.3). This approach, which regulates persistent motion through internal dynamics rather than explicit neighbor coupling, defines a broader class of self-aligning active matter, whose dynamics are captured by the framework of active Brownian particles with self-alignment [20, 48, 55]:

$$\dot{\mathbf{r}}_i = v_0\,\mathbf{n}_i + \mu \sum_{j\neq i} \mathbf{F}_{ij}, \tag{3.17}$$

$$\dot{\theta}_i = \sqrt{2D_R}\,\xi_i(t) - J\,\frac{\partial}{\partial\theta_i}\left(\mathbf{n}_i \cdot \hat{\mathbf{v}}_i\right), \tag{3.18}$$

where $\mathbf{n}_i = (\cos\theta_i, \sin\theta_i)$ is the polarity vector, and $\hat{\mathbf{v}}_i = \dot{\mathbf{r}}_i/|\dot{\mathbf{r}}_i|$ is the unit vector in the direction of motion. Here, v_0 is the self-propulsion speed, and μ is the mobility. The angular dynamics include Gaussian white noise $\xi_i(t)$ with strength D_R, satisfying $\langle \xi_i(t)\xi_j(t')\rangle = \delta_{ij}\delta(t-t')$, and a deterministic torque derived from the pseudo-potential $E_{\text{align}} = -J\,\mathbf{n}_i \cdot \hat{\mathbf{v}}_i$ [48, 55], which promotes alignment between the polarity and the direction of motion. The characteristic timescales $\tau_R = 1/D_R$ and $\tau = 1/J$ govern rotational diffusion and polarity realignment, respectively. The interaction force $\mathbf{F}_{ij}$ includes a short-range repulsion and a type-specific adhesive attraction. For interparticle distances $|\mathbf{r}_{ij}| \leq \sigma$, repulsion is modeled by $\mathbf{F}_{ij}^{\text{rep}} = -k_c(|\mathbf{r}_{ij}| - \sigma)\hat{\mathbf{r}}_{ij}$. For $\sigma < |\mathbf{r}_{ij}| \leq l_{\text{adh}}$, adhesion is described by $\mathbf{F}_{ij}^{\text{adh}} = -k_{\text{adh}}(|\mathbf{r}_{ij}| - \sigma)\hat{\mathbf{r}}_{ij}$, with adhesion strength depending on the pairwise identity. Here, $\hat{\mathbf{r}}_{ij} = \mathbf{r}_{ij}/|\mathbf{r}_{ij}|$, σ is the particle diameter, and l_{adh} is the interaction range.

Through large-scale simulations, Mones *et al.*[30] showed that the combination of self-alignment and differential adhesion leads to spontaneous segregation into large, coherent domains. The characteristic size scales as $R(t) \sim t^{\lambda}$ with $\lambda \approx 1$, implying $\overline{M}(t) \sim R^d(t) \sim t^2$ in two dimensions. This growth rate significantly surpasses that of classical coarsening regimes, such as Ostwald ripening ($z = 2/3$), diffusion-limited cluster aggregation ($z = 1/2$), and even ballistic aggregation ($z = 1$). These results demonstrate that collective motion significantly accelerates the aggregation process in cellular systems, as observed in the simulations by Belmonte *et al.* and experimentally by Méhes *et al.* [5, 44]. Despite these advances, the mechanistic origin of the anomalously fast coarsening exponents remained elusive. To address this, Beatrici *et al.* [31] proposed a theoretical framework showing that internal alignment within clusters modifies the scaling relation between cluster diffusivity and mass, $D \sim M^{\alpha}$, thereby altering the dynamic exponent z from that predicted by diffusion-limited cluster aggregation (DLCA). Their mean cluster approach analysis predicts $z = \frac{1}{1-\alpha}$ in two dimensions, a result confirmed by molecular dynamics simulations of self-propelled particles. However, their study was restricted to the regime of low alignment strength and remained within the DLCA paradigm, resulting in exponents in the range $1/2 \leq z \leq 1$. However, this is insufficient to explain the larger exponents observed in the experiments of Méhes *et al.* and in the simulations by Mones *et al.*.

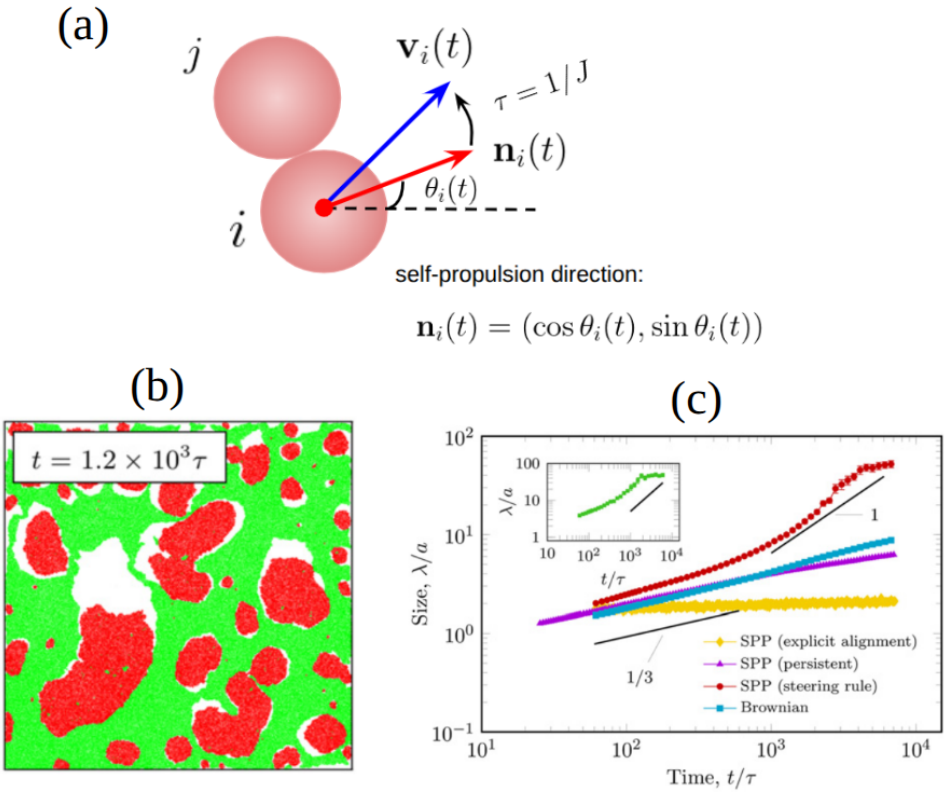

Figure 3.3: (a) Schematic representation of the self-alignment mechanism, in which each particle's polarity gradually aligns with its instantaneous velocity. (b) Snapshot from simulations of active disks with self-alignment and differential adhesion, showing spontaneous segregation of two cell types. (c) Temporal evolution of the characteristic domain size, exhibiting algebraic growth $R(t) \sim t^{\lambda}$ with exponent $\lambda \approx 1$ in the presence of self-alignment (red curve). This corresponds to an average cluster mass scaling $\overline{M}(t) \sim t^2$ in two dimensions. Adapted from Mones *et al.* [30].

To overcome these limitations, we performed extensive numerical simulations of adhesive self-propelled particles with a self-alignment mechanism to mimic cell aggregation in the segregation process. Based on these simulations and supported by analytical modeling, we proposed a generalized framework in which a flocking transition in the clusters of particles gives rise to collective ballistic aggregation. In this regime, internal alignment causes the cluster persistence length to grow faster with mass than the inter-cluster distance, enabling coherent and persistent cluster-level motion. This mechanism naturally explains the emergence of large coarsening exponents up to $z \simeq 2$, reconciling a wide range of experimental and numerical observations within a unified kinetic picture. Importantly, we showed that this ballistic regime is asymptotic—not transient—and arises from collective effects induced by internal alignment, distinguishing it from other ballistic scenarios driven solely by particle persistence. Our results offer a minimal yet predictive description of aggregation dynamics in active biological systems and help resolve long-standing discrepancies in the field. The main results obtained with this model were submitted to Physical Review Letters. The article, in its arXiv version, is included in Chapter 4 of this thesis. The arXiv version is available online at https://arxiv.org/abs/2508.11793.

Chapter 4

Article: Collective ballistic motion explains fast aggregation in adhesive active matter

Collective ballistic motion explains fast aggregation in adhesive active matter

Emanuel F. Teixeira,[1,*] P. de Castro,[2,†] Carine P. Beatrici,[1,‡]
Heitor C. M. Fernandes,[1,§] and Leonardo G. Brunnet[1,¶]

[1] *Instituto de Física, Universidade Federal do Rio Grande do Sul, CP 15051, CEP 91501-970 Porto Alegre - RS, Brazil*
[2] *ICTP South American Institute for Fundamental Research, Instituto de Física Teórica, UNESP – Universidade Estadual Paulista, Rua Dr. Bento T. Ferraz 271, 01140-070, São Paulo, SP, Brazil*

(Dated: August 19, 2025)

Inspired by motile cells during tissue formation, we identify a mechanism by which active systems of self-aligning adhesive particles undergo ballistic aggregation via a flocking transition. This kinetic regime emerges when the cluster persistence length grows faster with cluster mass than the intercluster distance does. We also characterize and explain the emergence of distinct non-collective kinetic regimes, including long-lived transients relevant to biological systems. Our results provide a unified framework consistent with the broad range of aggregation exponents experimentally observed in cellular systems and uncover physical principles which may enable timely tissue organization.

Introduction—Aggregation processes play a fundamental role in a wide range of systems, from colloidal suspensions and aerosols to biological matter [1–4]. In active systems such as swimming bacteria [5] and tissue cells [6], motile units interact and self-organize into growing clusters, driving key biological phenomena, including biofilm formation [7] and tissue development [8]. In particular, there has been long-standing interest in understanding tissue formation and cell sorting experiments [9–11]. These systems, characterized by strong cell–cell adhesion, exhibit a rich aggregation kinetics whose underlying principles remain poorly understood, despite their central role in timely tissue organization [12].

In the simplest theoretical description, cell clusters move diffusively with a diffusivity that decreases inversely with cluster mass, assuming uncorrelated self-propulsions of individual cells. This classical picture, known as diffusion-limited cluster aggregation (DLCA), predicts that the average cluster mass grows in time as $\overline{M}(t) \sim t^z$, with an aggregation exponent $z = 1/2$ in two dimensions [13–15]. In contrast, ballistic aggregation assumes persistent cluster motion. When combined with the assumption of uncorrelated self-propulsions—which causes the cluster speed to decay as the inverse square root of the cluster mass—the aggregation exponent becomes $z \simeq 1$ [16–18]. However, experiments in active tissues often report even faster coarsening dynamics with $z > 1$ [6, 12], indicating that classical models are insufficient.

Motivated by these discrepancies, Mones *et al.* [19] conducted simulations of adhesive active particles incorporating a self-alignment mechanism [20], where self-propulsion gradually aligns with net velocity, and observed an enhanced aggregation exponent $z \simeq 2$. This anomalously rapid coarsening was attributed to collective motion, similar to other works on Vicsek-like particles [14, 21]. Despite these findings, the mechanistic origin of this aggregation scaling remained unexplained. Subsequently, Beatrici *et al.* [22] showed how internal alignment in each cluster modifies the relation between cluster diffusivity and mass, thereby altering the coarsening exponent z. However, their analysis was limited to low alignment strength and low particle motion persistence, producing a modified DLCA with at most $z = 1$.

In this work, we demonstrate that the anomalous coarsening exponent $z \simeq 2$ fundamentally arises from a key mechanism: due to a flocking transition, the persistence length of cluster motion increases linearly with cluster mass while the inter-cluster distance increases with the square root of the cluster mass. This emergent behavior, driven by internal self-alignment among cluster constituents, induces a crossover from diffusive to collective ballistic dynamics as clusters grow. At high particle persistence time, we observe that a non-collective ballistic aggregation regime emerges even in the absence of self-alignment. Unlike the other regimes elucidated in the present work, we show that non-collective ballistic aggregation is a transient behavior. Nonetheless, convergence to DLCA occurs only at very late times, rendering the transient regime long-lived and relevant for biological systems, where particle numbers are far below Avogadro's number characteristic of molecular fluids.

By systematically tuning individual particle persistence and self-alignment strength in simulations of adhesive self-propelled particles, we explain the mechanisms behind the broad range of experimentally observed aggregation exponents. Our results are supported by a combination of detailed single-cluster analyses and a generalized Smoluchowski coagulation theory [23]. Together, these findings unify previously disconnected experimental and theoretical observations and reveal how cooperative mechanisms fundamentally reshape aggregation kinetics in living matter.

Model—To investigate cluster aggregation in adhesive active matter with alignment, we employ a minimal model inspired by motile tissue cells [24]. Particles are

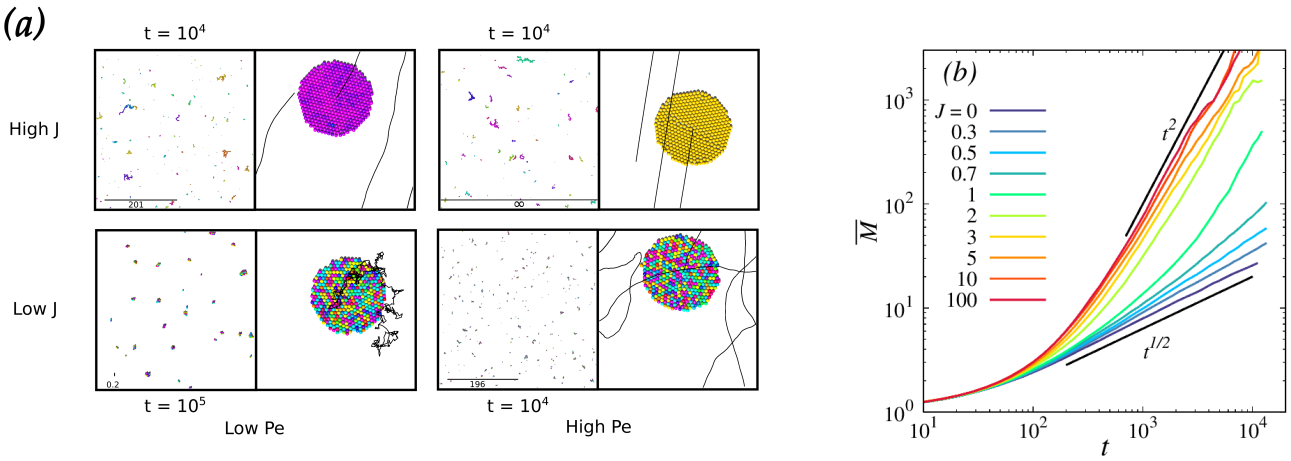

FIG. 1. Adhesive active matter exhibits rich aggregation dynamics tuned by self-alignment. (a) Typical snapshots for kinetic regimes with high and low self-alignment (J) and Péclet number (Pe). In each case, the left panels show simulations of adhesive particle aggregation where the bar indicates the typical cluster persistence length. The right panels show single-cluster simulations with lines representing the cluster's trajectory. (b) Time dependence of the average cluster mass $\overline{M}(t)$ for multiple values of J, demonstrating that stronger alignment interactions accelerate the aggregation dynamics and correspondingly increase aggregation exponents. Here, Pe = 1.

represented as disks subject to contact forces and self-alignment: each particle self-propels along a noisy direction that gradually aligns with its own net velocity. A strong attractive force accounts for cell adhesion. Despite its simplicity, the model reproduces key features of collective migration and aggregation. Self-alignment induces collective motion (as discussed below) and is more realistic in this context than the original Vicsek alignment [25], since tissue cells cannot explicitly average over neighbors [24]. Nonetheless, our results are expected to be robust to the choice of alignment rule, as observed for Vicsek-like alignment at low strength [22].

We consider N adhesive active Brownian disks in 2D with periodic boundary conditions [24, 26]. Their overdamped dynamics is given by:

$$\dot{\mathbf{r}}_i = v_0\,\mathbf{n}_i + \mu \sum_{j\neq i} \mathbf{F}_{ij}, \tag{1}$$

$$\dot{\theta}_i = \sqrt{2D_R}\,\xi_i - J\frac{\partial}{\partial\theta_i}\left(\mathbf{n}_i\cdot\hat{\mathbf{v}}_i\right), \tag{2}$$

where v_0 is the self-propulsion speed, $\mathbf{n}_i = (\cos\theta_i, \sin\theta_i)$ is the self-propulsion direction, also called polarity, ξ_i is a Gaussian white noise with $\langle\xi_i(t)\xi_j(t')\rangle = \delta_{ij}\delta(t-t')$ and $\hat{\mathbf{v}}_i = \mathbf{v}_i/|\mathbf{v}_i|$, where $\mathbf{v}_i = \dot{\mathbf{r}}_i$. The parameters D_R and J set the reorientation timescales $\tau_R = 1/D_R$ and $\tau = 1/J$, respectively. The alignment term has a pseudo potential $E_{\text{align}} = -J\,\mathbf{n}_i\cdot\hat{\mathbf{v}}_i$ [27, 28]. The contact interaction force $\mathbf{F}_{ij}$ between particles i and j comprises a short-range repulsion and a short-range adhesion. For interparticle distances $|\mathbf{r}_{ij}| \leq \sigma$, a repulsive force $\mathbf{F}_{ij}^{\text{rep}} = -k_c\left(|\mathbf{r}_{ij}| - \sigma\right)\hat{\mathbf{r}}_{ij}$ penalizes overlap between the disks, such that their diameter is σ. In the range $\sigma < |\mathbf{r}_{ij}| \leq l_{\text{adh}}$, an adhesive force $\mathbf{F}_{ij}^{\text{adh}} = -k_{\text{adh}}\left(|\mathbf{r}_{ij}| - \sigma\right)\hat{\mathbf{r}}_{ij}$ attracts neighboring particles. Here, $\hat{\mathbf{r}}_{ij} = \mathbf{r}_{ij}/|\mathbf{r}_{ij}|$ is the unit vector connecting the centers of particles i and j, σ is the particle diameter, and l_{adh} sets the adhesive interaction range.

We measure spatial coordinates and time in units of σ and $\tau_0 = \sigma/v_0$, respectively. In that spirit, we express the decorrelation time of the polarity, τ_R, as the (rotational) Péclet number [29, 30], $\text{Pe} \equiv v_0\tau_R/\sigma = \tau_R/\tau_0$. We start from a random initial condition and let the system evolve into growing clusters by merger events where particles irreversibly adhere. Unless otherwise specified, all simulations employ $N = 4\times10^4$ particles. To suppress multi-cluster merger events and percolation effects, we use a low packing fraction, $\phi = 0.01$. This produces slower aggregation kinetics (without altering the exponents) in which the cluster-mass distribution evolves more smoothly and the power-law regime is extended in time, thereby improving statistics. We also performed tests at moderately higher ϕ and confirmed that the same exponents can be observed. Other simulation details are provided in the Supplemental Material [31].

Low particle persistence—First, we consider how self-alignment affects aggregation in the low-Pe regime (Pe = 1). Fig. 1a shows that aggregation proceeds faster for higher J. To quantify this, Fig. 1b shows the observed power-law behavior of the average cluster mass versus time, $\overline{M}(t) \sim t^z$, which sets in after some time. Between $J = 0$ and $J \approx 0.7$, the aggregation exponent changes from $z = 1/2$ to $z = 1$. Upon further increasing J, z jumps to $z \approx 2$.

To fully understand how z changes due to J, we need to understand how particles interact within clusters and how each cluster moves as a result. For that, we simu-

lated a single isolated cluster. To quantify internal collectivity, that is, the level of alignment among polarities in a cluster, we use the global polar order parameter $\Psi = \left\langle \left| \sum_i^M \mathbf{n}_i \right| \right\rangle_t / M$, where $\langle ... \rangle_t$ represents steady state average [29]. High (low) collectivity implies $\Psi \to 1$ ($\Psi \to 0$). Figure 2a displays Ψ versus J for different cluster masses, showing that J induces polar order [5, 24, 25, 29]. The difference in Ψ between order and disorder increases with cluster mass. Polar order emerges here as follows. Particles adhere and have therefore to move together, with similar velocities. At strong J, particles eventually self-align with their common velocity.

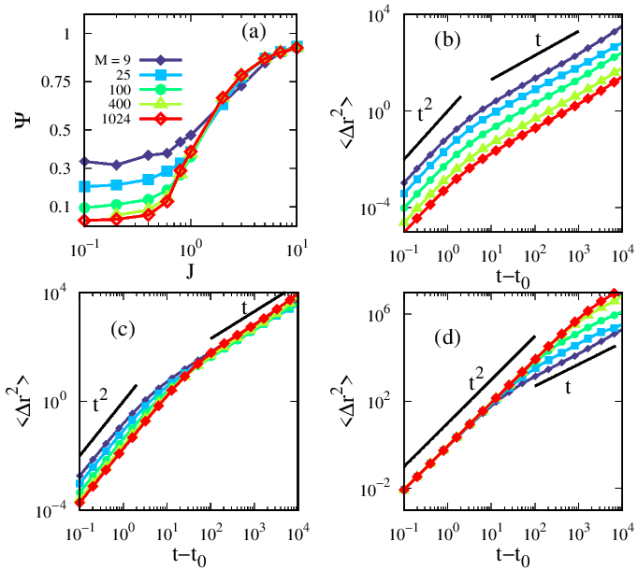

FIG. 2. Self-alignment makes single cluster of adhesive active particles undergo a collective motion transition, altering the duration and intensity of the ballistic regime as well as the effect of cluster mass on motion. (a) Collectivity order parameter Ψ versus self-alignment strength J for different cluster masses. A transition from disorder to collective motion order occurs around $J \approx 0.6$. $\langle \Delta r^2 \rangle (t)$ for a single cluster is shown for different cluster masses (b) in the disordered regime at $J = 0$, (c) near the transition at $J = 0.6$, and (d) above the transition to collective motion at $J = 10$. In all curves here, Pe = 1.

To understand the resulting single-cluster motion, we measure the cluster's mean square displacement $\langle \Delta r^2 \rangle = \left\langle (\mathbf{r}_{\rm cm}(t) - \mathbf{r}_{\rm cm}(t_0))^2 \right\rangle$, where $\mathbf{r}_{\rm cm}$ is the cluster's center of mass position and $\langle ... \rangle$ represents averaging over time windows. All curves in Figs. 2b-d are well fitted by the analytical expression for an active Brownian particle, $\langle \Delta r^2 \rangle = 2V_c^2 \tau_p \left[t - \tau_p \left(1 - e^{t/\tau_p} \right) \right]$, where V_c is the effective self-propulsion speed of the cluster and τ_p is the persistence time of the cluster [32–35]. At short times $t \ll \tau_p$, the cluster moves in a ballistic regime, where $\langle \Delta r^2 \rangle \approx V_c^2 t^2$. At long times $t \gg \tau_p$, the regime is normal diffusion, with $\langle \Delta r^2 \rangle \approx 2V_c^2 \tau_p t$.

For $J = 0$ (Fig. 2b), $\langle \Delta r^2 \rangle (t)$ decreases with cluster mass in both ballistic and diffusive regimes. Without alignment, polarities may oppose each other (see Fig. 1a). The chance of two cells pushing in opposite directions grows with mass. The persistence time τ_p equals the single-particle value τ_R and is mass-independent, since for $J = 0$ reorientations are unaffected by particle-particle interactions. Near the flocking transition ($J \approx 0.6$, Fig. 2c), the ballistic regime remains slower for larger clusters, but alignment suppresses fluctuations and increases τ_p with mass. This compensation yields convergence of all $\langle \Delta r^2 \rangle (t)$ curves at long times, where they become mass-independent. Above the transition ($J = 10$, Fig. 2d), particles align their polarities (see Fig. 1a), and clusters move coherently at nearly v_0, making V_c mass-independent. Larger clusters retain longer τ_p, so the long-time $\langle \Delta r^2 \rangle$ now increases with mass.

We quantify how the effective active cluster motion parameters depend on cluster mass. Figure 3a shows V_c versus mass for various values of J. For small J, the speed decays as $V_c \sim M^\gamma$ with $\gamma \simeq -1/2$, consistent with the idea that the average of M independent stochastic contributions scales as $1/\sqrt{M}$. As J increases, γ also increases, reaching $\gamma = 0$, where $V_c = v_0$. Figure 3b shows the cluster persistence time τ_p versus mass. As J increases, τ_p grows algebraically with mass, $\tau_p \sim M^\nu$, with ν increasing from 0 to approximately 1. The long-time diffusion coefficient is $D = V_c^2 \tau_p / 2$, so $D \sim M^\alpha$, where $\alpha = 2\gamma + \nu$. Fig. 3c shows that $-1 \leq \alpha \leq 1$. For low (high) J, D decreases (increases) with mass.

To characterize the aggregation regime, we compare the average inter-cluster distance, $\bar{l}_c$, with the clusters' persistence length, $l_p = V_c \tau_p$. If clusters collide and merge before traveling a persistence length, the aggregation occurs in the ballistic regime. Conversely, if clusters travel a distance larger than l_p before merging, the process is a diffusion-limited cluster aggregation (DLCA). The average inter-cluster distance $\bar{l}_c$ is estimated from the global particle density $\rho = N/L^2$ and the average cluster mass $\overline{M}$ via the relation $\bar{l}_c = \sqrt{\overline{M}/\rho}$ [22].

Figure 3d shows that $l_p(M) \sim M^\delta$, with $\delta = \nu + \gamma$. Applying for $M = \overline{M}$, we define $\bar{l}_p(\overline{M}) \sim \overline{M}^\delta$ which we then compare to $\bar{l}_c$ to identify the aggregation regime. For a ballistic collision, each cluster must travel a distance at least on the order of the persistence length l_p. Therefore, if the clusters are initially separated by a distance l_c, the ballistic condition reads $2l_p/l_c > 1$.

Fig. 3e shows $2\bar{l}_p/\bar{l}_c$ versus $\overline{M}$. For $J \geq 2$, the curves cross the criterion $2\bar{l}_p/\bar{l}_c = 1$ at $\overline{M} \approx 10^2$, indicating a ballistic aggregation regime for large masses consistent with the faster kinetics observed for $\overline{M}$ in Fig 1b. For lower, intermediate values of J in the range $0.8 \leq J \leq 1$, the ratio $2\bar{l}_p/\bar{l}_c$ is expected to cross 1 at larger $\overline{M}$, suggesting that ballistic behavior emerges only at later

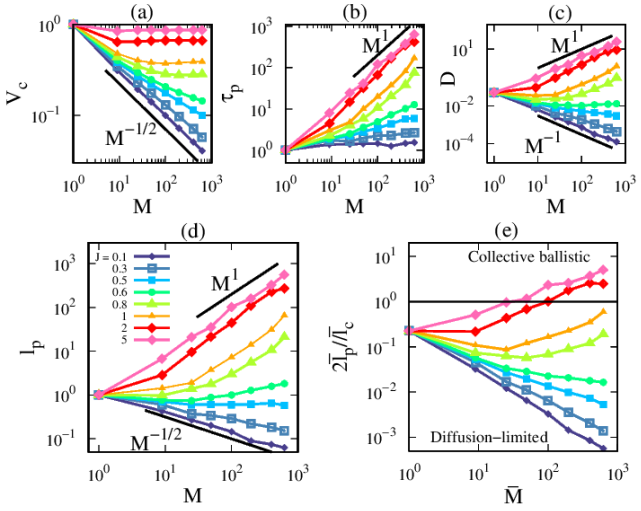

FIG. 3. Self-alignment fundamentally changes how the speed, persistence and diffusion of a single cluster depend on its mass, explaining aggregation kinetics regimes. For different alignment strengths J, the dependence on cluster mass is shown for (a) cluster speed V_c, (b) cluster persistence time τ_p, (c) effective diffusion coefficient $D = V_c^2\tau_p/2$, where self-alignment induces transition from mass-hindered to mass-enhanced diffusion, (d) persistence length $l_p = V_c\tau_p$, and (e) kinetic regime criterion ratio $2\bar{l}_p/\bar{l}_c$. A crossover from diffusion-limited to ballistic aggregation occurs as $2\bar{l}_p/\bar{l}_c$ exceeds unity.

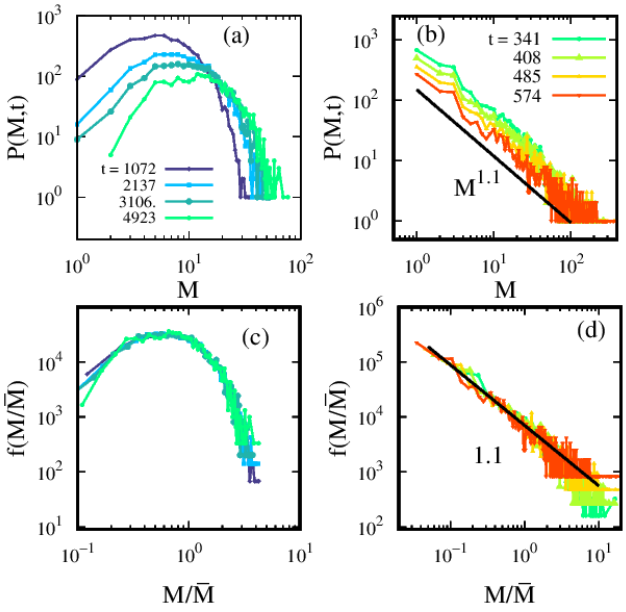

FIG. 4. Cluster mass distribution exhibits power-law behavior induced by self-alignment as well as universal dynamical scaling in both the collective and the non-collective regimes. (a) Cluster mass distribution $P(M,t)$ versus M at different times for $J = 0$, below the flocking transition, showing a non-monotonic shape. (b) For $J = 10$, above the collective transition, the distribution becomes $P(M,t) \sim M^{-\lambda}$ with $\lambda \simeq 1.1$. (c–d) Data collapse of the rescaled mass distributions onto a single universal dynamic scaling function $f\left(M/\overline{M}\right) = \overline{M}^2 P(M,t)$ [17].

times. This is also consistent with our measurements in Fig. 1b, where the aggregation exponent of $\overline{M}$ exhibits a crossover to a faster aggregation regime with $z \simeq 2$. In contrast, for $J \leq 0.6$, the ratio $2\bar{l}_p/\bar{l}_c$ remains below 1 for all mass values, indicating that the system is in the DLCA regime throughout the whole aggregation process.

Therefore, the observed increase in the exponent z in Fig. 1b signals a shift from DLCA to ballistic aggregation. This shift is driven by collective motion within clusters, above which the persistence length grows linearly with the average mass while the ratio $\bar{l}_p/\bar{l}_c$ scales as $\sim \overline{M}^{1/2}$. At sufficiently large $\overline{M}$, the ballistic aggregation criterion is satisfied. Crucially, collective ballistic aggregation is the asymptotic regime, not a transient effect.

We also analyze the impact of J on the full cluster mass distribution $P(M,t)$ [36], whose relevance will become clear in the analytical approach employed below. Figures 4a–b show $P(M,t)$ once the system reaches the algebraic aggregation regime. For $J = 0$, the distribution has a peak. For $J = 100$, a power law $P(M,t) \sim M^{-\lambda}$ emerges, with $\lambda \simeq 1.1$. Importantly, as shown in Figs. 4c–d, the distributions display dynamical scaling: all curves collapse onto a single universal function, $f\left(M/\overline{M}\right) = \overline{M}^2 P(M,t)$, as observed in other problems of irreversible aggregation [17, 37].

In order to quantitatively explain the aggregation exponent z in each aggregation kinetics regime, we develop an analytical approach based on the Smoluchowski coagulation equation, a master-equation-like set of differential equations for the number of clusters with a given mass; see Supplementary Material [31]. In the DLCA regime, we adopt an aggregation rate proportional to the sum of the diffusion coefficients of the merging clusters, $K(M,M') \sim D(M) + D(M')$, which corresponds to the Brownian kernel in two dimensions [17, 38–40]. Taking into account the dynamic scaling of the mass distribution just observed, we obtain an algebraic solution for the average cluster mass with exponent $z = \frac{1}{1-\alpha}$. Since we find $-1 \leq \alpha \leq 0$ for DLCA, this yields $\frac{1}{2} \leq z \leq 1$, in agreement with our simulations.

A similar approach is applied for the ballistic aggregation regime. In this case, we use the well-established ballistic kernel given by $K(M,M') \sim |V_c(M) - V_c(M')|\,(R(M) + R(M'))$, where $R(M) \sim M^{1/2}$ is the average cluster radius, which in turn appears because cluster cross section matters when aggregation is rapid [17]. This leads to $z = \frac{2}{1-2\gamma}$ as discussed in the Supplementary Material [31]. As shown in Fig. 3a, for $J \geq 0.8$, the system exhibits ballistic aggregation with mass-independent cluster speed ($\gamma = 0$), resulting in $z = 2$, consistent with our simulations.

High particle persistence and diagram—For high Pe = 10^3 and $J = 0$, a non-collective ballistic cluster motion emerges. Fig. 5a shows that the average cluster mass grows algebraically with $z \simeq 1$. As in the ballistic regime with low Pe and $J = 0$, for high Pe we also observed that $V_c \sim M^{-1/2}$ and $\tau_p = \tau_R$ is mass independent (see again Fig. 3a-b). This is expected since increasing Pe does not affect particle-particle interactions. Consequently, for Pe $= \tau_p/\tau_0 = 10^3$, we have $\bar{l}_p \sim 10^3/\sqrt{\overline{M}}$ and $2\bar{l}_p/\bar{l}_c \simeq 225.73\,\overline{M}^{-1}$. Thus, $\overline{M} < 225.73$ yields ballistic aggregation, whereas larger masses are DLCA. The first power-law regime that emerges during ballistic aggregation is also important as long-lived transients are relevant in biological systems due to the not-so-large number of particles. Using these observations in Smoluchowski theory [31] gives $z = 1$, matching the simulations.

At high Pe, as J increases, our simulations show that $l_p \sim M$ and, as a consequence, $2\bar{l}_p/\bar{l}_c \sim \overline{M}^{1/2} > 1$, indicating the ballistic aggregation regime. Again, since the cluster speed becomes mass-independent ($\gamma = 0$) as seen in Fig. 3a, Smoluchowski theory predicts an exponent $z = 2$, consistent with our simulations. For both low and high particle persistence, we refer to this regime as *collective ballistic aggregation*, as the ballistic aggregation kinetics arises from persistent and coherent cluster-level motion.

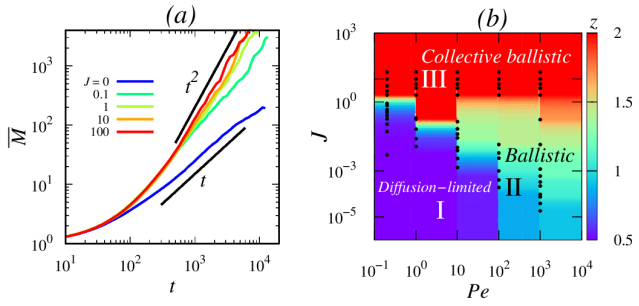

FIG. 5. High persistence enables non-collective ballistic aggregation with exponent $z = 1$, completing the rich set of aggregation regimes. (a) Average cluster mass versus time for different self-alignment strengths J at Pe $= 10^3$. We observe $\overline{M}(t) \sim t^z$, with $z \simeq 1$ even for $J = 0$, indicating non-collective ballistic aggregation. Unlike collective ballistic aggregation, this is a long-lived transient regime (relevant for biological systems) which eventually changes to DLCA for large masses and times. (b) Aggregation regime diagram showing the aggregation exponent z. Region I (blue) is diffusion-limited cluster aggregation (DLCA); Region II (light blue) is ballistic aggregation driven by persistence; Region III (red) represents collective ballistic aggregation induced by internal alignment.

To summarize the aggregation regimes, we present in Fig. 5b a diagram in the plane Pe versus J, identifying three distinct regions based on the aggregation exponent z. For low J and Pe, the system exhibits diffusion-limited cluster aggregation (DLCA), labelled as Region I. For low J and high Pe, the aggregation is ballistic due to enhanced persistence without collective effects, defining Region II. Finally, for high J, flocking behavior within clusters induces coherent motion and leads to collective ballistic aggregation, corresponding to Region III.

Conclusions—We presented a comprehensive theoretical and computational analysis elucidating the mechanisms by which collective motion enables fast cluster aggregation in active biological systems. By tuning the alignment interaction strength J and the Péclet number Pe, we identified distinct aggregation regimes and established the scaling behavior of the average cluster mass $\overline{M}(t) \sim t^z$, with the aggregation exponent z ranging from 1/2 to 2. Through a detailed single-cluster analysis, we uncovered how the persistence length $l_p \sim M^\delta$ emerges from the interplay between alignment and cluster size.

At low J, clusters lack coherent motion and behave diffusively, with persistence length decreasing with size, leading to diffusion-limited cluster aggregation (DLCA) [13, 15]. In this regime, both numerical simulations and Smoluchowski theory yield aggregation exponents $z \in [1/2, 1]$, consistent with classical DLCA models. As J increases, internal alignment promotes coherent motion within clusters. This induces a transition to a ballistic regime, characterized by a growing persistence length and enhanced collision rates. When $2l_p/l_c$ exceeds unity, aggregation becomes ballistic, with mass-independent cluster velocities ($\gamma = 0$) yielding $z \approx 2$. We term this regime *collective ballistic aggregation*, as the ballistic character emerges from internally generated alignment rather than from self-propulsion alone. Notably, this regime is asymptotic, not transient, producing aggregation exponents distinct from diffusive regimes. This elucidation may resolve anomalous aggregation results reported in prior studies [6, 19].

We further explored the role of persistence by increasing Pe, showing that even without alignment ($J = 0$), high persistence leads to ballistic aggregation in a long-lived transient relevant to biological systems. This behavior eventually transitions to DLCA because the average cluster mass increases and persistence becomes insufficient to maintain ballistic encounters. By combining theory and simulations, we constructed a diagram in the Pe–J plane that summarizes the aggregation regimes.

Our framework not only clarifies how alignment and persistence shape the aggregation dynamics in active systems, but also provides predictive insights relevant to biological contexts such as tissue formation, where cell motility and collective behavior are tightly coupled. Moreover, the mechanisms elucidated here become a strong candidate to explain the diversity of aggregation exponents found in experiments. Future work should aim to determine model parameters experimentally to assess the degree of realism of our framework. Another avenue is to examine cluster fragmentation, which may be sig-

nificant for some types of cells. Finally, additional properties of the surrounding medium such as viscoelasticity [41] and contact inhibition interactions with certain cell types [11] could also modulate aggregation kinetics.

We express our gratitude to the Brazilian agencies CAPES, CNPq, FAPERGS and FAPESP for their financial support. H.C.M.F. and L.G.B. acknowledge the support from the National Council for Scientific and Technological Development – CNPq (procs. 402487/2023-0 and 443517/2023-1). E.F.T. acknowledges ICTP-SAIFR/IFT-UNESP. The simulations were conducted using the VD Lab cluster infrastructure at IF-UFRGS. P.d.C. was supported by Scholarships No. 2021/10139-2 and No. 2022/13872-5 and ICTP-SAIFR Grant No. 2021/14335-0, all granted by São Paulo Research Foundation (FAPESP), Brazil.

* emanuel.teixeira@ufrgs.br
† pablo.castro@unesp.br
‡ carine@if.ufrgs.br
§ heitor.fernandes@ufrgs.br
¶ leon@if.ufrgs.br

[1] A. A. Hyman, C. A. Weber, and F. Jülicher, Annual review of cell and developmental biology **30**, 39 (2014).
[2] S. V. Franklin and M. D. Shattuck, *Handbook of granular materials* (CRC Press, 2016).
[3] P. de Castro, F. Urbina, A. Norambuena, and F. Guzmán-Lastra, Physical Review E **108**, 044104 (2023).
[4] C. B. Caporusso, L. F. Cugliandolo, P. Digregorio, G. Gonnella, D. Levis, and A. Suma, Physical Review Letters **131**, 068201 (2023).
[5] F. Peruani, J. Starruß, V. Jakovljevic, L. Søgaard-Andersen, A. Deutsch, and M. Bär, Physical review letters **108**, 098102 (2012).
[6] O. Cochet-Escartin, T. T. Locke, W. H. Shi, R. E. Steele, and E.-M. S. Collins, Biophysical journal **113**, 2827 (2017).
[7] G. O'Toole, H. B. Kaplan, and R. Kolter, Annual Reviews in Microbiology **54**, 49 (2000).
[8] N. C. Heer and A. C. Martin, Development **144**, 4249 (2017).
[9] S. G. Krens and C.-P. Heisenberg, Current topics in developmental biology **95**, 189 (2011).
[10] E. F. Teixeira, C. P. Beatrici, H. C. Fernandes, and L. G. Brunnet, Physical Review Letters **134**, 138401 (2025).
[11] M. Bothe, E. Lardet, A. Poliakov, G. Pruessner, T. Bertrand, and I. Bordeu, arXiv preprint arXiv:2503.13714 (2025).
[12] E. Méhes, E. Mones, V. Nemeth, and T. Vicsek, PloS one **7**, e31711 (2012).
[13] A. Nakajima and S. Ishihara, New Journal of Physics **13**, 033035 (2011).
[14] P. Cremer and H. Löwen, Physical Review E **89**, 022307 (2014).
[15] M. Durand, Plos Computational Biology **17**, e1008576 (2021).
[16] Y. Jiang and F. Leyvraz, Journal of Physics A: Mathematical and General **26**, L179 (1993).
[17] F. Leyvraz, Physics Reports **383**, 95 (2003).
[18] P. L. Krapivsky, S. Redner, and E. Ben-Naim, *A kinetic view of statistical physics* (Cambridge University Press, 2010).
[19] E. Mones, A. Czirók, and T. Vicsek, New journal of physics **17**, 063013 (2015).
[20] P. Baconnier, O. Dauchot, V. Démery, G. Düring, S. Henkes, C. Huepe, and A. Shee, Reviews of Modern Physics **97**, 015007 (2025).
[21] T. Paul, N. Vadakkayil, and S. K. Das, Physical Review E **109**, 064607 (2024).
[22] C. P. Beatrici, R. M. de Almeida, and L. G. Brunnet, Physical Review E **95**, 032402 (2017).
[23] M. v. Smoluchowski, Z. Physik. **17**, 585 (1916).
[24] B. Szabo, G. Szöllösi, B. Gönci, Z. Jurányi, D. Selmeczi, and T. Vicsek, Physical Review E **74**, 061908 (2006).
[25] T. Vicsek, A. Czirók, E. Ben-Jacob, I. Cohen, and O. Shochet, Physical review letters **75**, 1226 (1995).
[26] S. Henkes, Y. Fily, and M. C. Marchetti, Physical Review E—Statistical, Nonlinear, and Soft Matter Physics **84**, 040301 (2011).
[27] D. Sarkar, G. Gompper, and J. Elgeti, Communications Physics **4**, 36 (2021).
[28] D. L. Barton, S. Henkes, C. J. Weijer, and R. Sknepnek, PLoS computational biology **13**, e1005569 (2017).
[29] A. Martín-Gómez, D. Levis, A. Díaz-Guilera, and I. Pagonabarraga, Soft matter **14**, 2610 (2018).
[30] Y. Zhao, T. Ihle, Z. Han, C. Huepe, and P. Romanczuk, Physical Review E **104**, 044605 (2021).
[31] See Supplemental Material at [URL will be inserted by publisher] for videos and analytical details, which includes Refs. [17, 18, 22, 23, 38–40].
[32] Y. Fily and M. C. Marchetti, Physical review letters **108**, 235702 (2012).
[33] Y. Fily, S. Henkes, and M. C. Marchetti, Soft matter **10**, 2132 (2014).
[34] M. C. Marchetti, Y. Fily, S. Henkes, A. Patch, and D. Yllanes, Current Opinion in Colloid & Interface Science **21**, 34 (2016).
[35] A. Villa-Torrealba, C. Chávez-Raby, P. de Castro, and R. Soto, Physical Review E **101**, 062607 (2020).
[36] P. de Castro, S. Diles, R. Soto, and P. Sollich, Soft Matter **17**, 2050 (2021).
[37] M. Kolb, Physical review letters **53**, 1653 (1984).
[38] A. Moncho-Jordá, F. Martínez-López, M. Quesada-Pérez, M. Cabrerizo-Vílchez, and R. Hidalgo-Álvarez, Surface and Colloid Science , 113 (2004).
[39] A. Moncho-Jordá, F. Martınez-López, and R. Hidalgo-Álvarez, Physica A: Statistical Mechanics and its Applications **282**, 50 (2000).
[40] A. Moncho-Jordá, G. Odriozola, F. Martınez-López, A. Schmitt, and R. Hidalgo-Álvarez, The European Physical Journal E **5**, 471 (2001).
[41] D. A. Beysens, G. Forgacs, and J. A. Glazier, Proceedings of the National Academy of Sciences **97**, 9467 (2000).

Supplementary Material: Collective ballistic motion explains fast aggregation in adhesive active matter

CLUSTER MASS DISTRIBUTIONS AND DYNAMICAL SCALING AT HIGH PÉCLET NUMBER

We present here our results for the effect of the alignment strength J on the cluster mass distribution $P(M,t)$ in the high Péclet number regime ($\mathrm{Pe} = 10^3$). Figures S1a and b show $P(M,t)$ for different time instants after the system has entered the algebraic coarsening regime. The behavior is to that presented for low Péclet number in the main text. For $J = 0$, below the flocking transition, the distribution exhibits a non-monotonic shape, indicating the presence of a characteristic cluster size. In contrast, for strong alignment ($J = 100$), the distribution develops a power-law tail, $P(M,t) \sim M^{-\lambda}$, with exponent $\lambda \simeq 1.1$, consistent with scale-free cluster growth driven by collective motion. We observe in Figures S1c and d that the distributions obey dynamical scaling. When rescaled by the mean cluster mass $\overline{M}(t)$, all curves collapse onto a single universal function, $f\left(\frac{M}{\overline{M}}\right) = \overline{M}^2 P(M,t)$, demonstrating self-similar evolution during the coarsening process. The same universal scaling function was observed in Ref. [S17] for another irreversible aggregation problem.

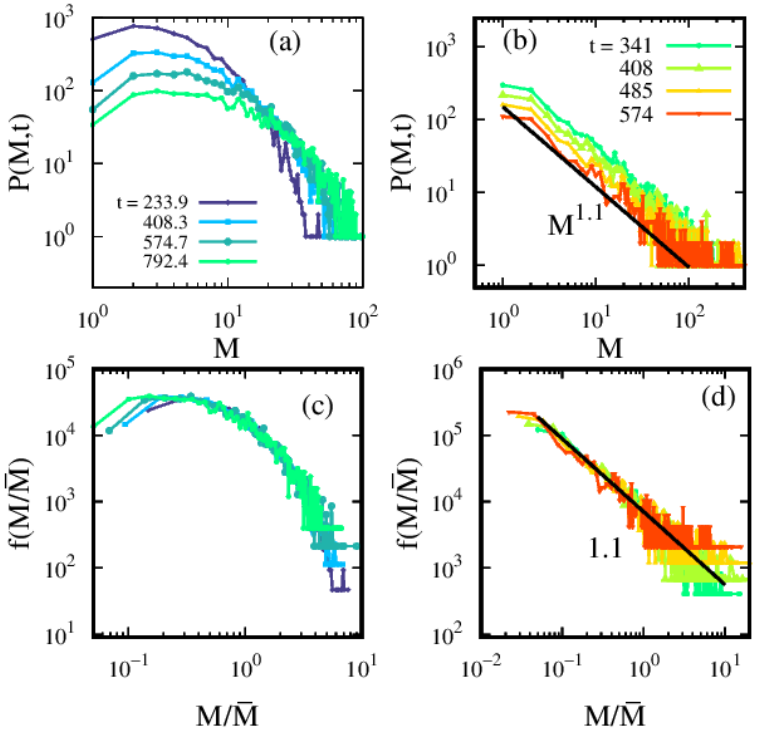

FIG. S1. **Figure S1.** Cluster mass distribution $P(M,t)$ in the high Péclet number regime ($\mathrm{Pe} = 10^3$). (a) For $J = 0$, below the flocking threshold, the distribution has a peak, reflecting a characteristic cluster size. (b) For $J = 100$, above the flocking transition, the distribution becomes power-law, $P(M,t) \sim M^{-\lambda}$, with $\lambda \simeq 1.1$. For (c) $J = 0$ and (d) $J = 100$, the rescaled distributions collapse onto a single curve, $f(M/\overline{M}) = \overline{M}^2 P(M,t)$, confirming dynamical scaling [S17].

ADDITIONAL SIMULATION DETAILS

Throughout this work, we use $k_c = 200 v_0/(\sigma\mu)$, $k_{\mathrm{adh}} = 10 v_0/(\sigma\mu)$, $v_0 = 0.1$, $\mu = 1$, $\sigma = 1$ and $l_{\mathrm{adh}} = 1.5\sigma$. This choice of parameters guarantees k_{adh} sufficiently large to cause particles to irreversibly bind when they encounter each other. In fact, the lowest adhesion force, $k_{\mathrm{adh}}\sigma$, is 10 times larger than the self-propulsion force v_0/μ, so particles will move only in directions that do not destroy binding. We integrate the equations of motion using the Euler-Maruyama algorithm with a time step $\Delta t = 0.001\tau_0$.

CLUSTER AGGREGATION THEORY: THE SMOLUCHOWSKI COAGULATION EQUATION

We present here a cluster aggregation theory based on the Smoluchowski coagulation equation [S23] generalized to the types of mass-dependent cluster movements of our problem. This theoretical approach builds on the derivation presented in Ref. [S17], incorporating modifications where appropriate. For completeness, we include intermediate steps common to other irreversible aggregation problems. Consider clusters with different masses moving through space. When two clusters of masses M and M' come sufficiently close, they may irreversibly merge into a single cluster of mass $M + M'$:

$$A_M + A_{M'} \xrightarrow[K(M,M')]{} A_{M+M'}. \tag{S1}$$

Here, A_M denotes a cluster and $K(M, M')$ denotes the rate at which two clusters of masses M and M' coagulate. This quantity is known as the coagulation kernel.

We assume a continuous mean-field approach characterized by spatial homogeneity, where the cluster mass distribution is uniform throughout the entire space:

$$\int_{V_0} P(\mathbf{r}, M, t)\, dV = P(M, t)V_0, \tag{S2}$$

where $P(M, t)$ is the spatially-homogeneous cluster mass distribution and $V_0 = L^d$ is the total d-dimensional hypercubic volume. Notice that, while our simulations were performed in $d = 2$, consistent with many experimental setups, we formulate the theory in arbitrary dimension d, as the generalization is straightforward. We now define the concentration of the mass distribution as

$$C(M, t) = \frac{P(M, t)}{V_0}. \tag{S3}$$

The concentration $C(M, t)$ increases when two smaller clusters of masses M' and $M - M'$ merge to form a cluster of mass M. The rate of this process is proportional to the product $C(M', t)\, C(M - M', t)$. On the other hand, when a cluster of mass M merges with any other cluster, it is removed from the population, resulting in a decrease in $C(M, t)$. To describe the full aggregation process, we integrate over the coagulating masses, treated as continuous variables:

$$\frac{\partial C(M,t)}{\partial t} = \frac{1}{2}\int_0^M K(M', M - M')\, C(M', t)\, C(M - M', t)\, dM' - \int_0^\infty K(M, M')\, C(M, t)\, C(M', t)\, dM', \tag{S4}$$

where $K(M, M')$ is the coagulation kernel. The prefactor $1/2$ ensures that the contribution is not double-counted. Equation (S4) is the Smoluchowski coagulation equation [S23]. In terms of the mass distribution $P(M, t)$, Eq. (S4) becomes

$$\frac{\partial P(M,t)}{\partial t} = \frac{1}{2\,V_0}\int_0^M K(M', M - M')\, P(M', t)\, P(M - M', t)\, dM' - \frac{1}{V_0}\int_0^\infty K(M, M')\, P(M, t)\, P(M', t)\, dM'. \tag{S5}$$

We note that the total mass is conserved:

$$M_0 = \int_0^\infty M\, P(M, t)\, dM = \text{const}. \tag{S6}$$

Also, we define the total number of clusters:

$$N(t) = \int_0^\infty P(M, t)\, dM. \tag{S7}$$

Using Eq. (S5), we compute the time derivative of $N(t)$:

$$\begin{aligned}\frac{dN(t)}{dt} \;=\; & \frac{1}{2\,V_0}\int_0^\infty\int_0^M K(M', M - M')\, P(M', t)\, P(M - M', t)\, dM'\, dM \\ & -\frac{1}{V_0}\int_0^\infty\int_0^\infty K(M, M')\, P(M, t)\, P(M', t)\, dM'\, dM.\end{aligned} \tag{S8}$$

We now interchange the order of integration in the first term and perform the change of variables $M'' = M - M'$:

$$\begin{aligned}\frac{dN(t)}{dt} &= \frac{1}{2\,V_0}\int_0^\infty\int_0^\infty K(M',M'')P(M',t)P(M'',t)\,dM''\,dM' \\ &\quad -\frac{1}{V_0}\int_0^\infty\int_0^\infty K(M,M')P(M,t)P(M',t)\,dM'\,dM. \end{aligned} \tag{S9}$$

Renaming dummy variables $M' \to M$ and $M'' \to M'$, this becomes

$$\frac{dN(t)}{dt} = -\frac{1}{2\,V_0}\int_0^\infty\int_0^\infty K(M,M')P(M,t)P(M',t)\,dM'\,dM. \tag{S10}$$

The average cluster mass is defined as

$$\overline{M}(t) = \frac{\int_0^\infty MP(M,t)\,dM}{\int_0^\infty P(M,t)\,dM} = \frac{M_0}{N(t)}. \tag{S11}$$

Thus,

$$N(t) = \frac{M_0}{\overline{M}(t)}. \tag{S12}$$

Taking the time derivative yields

$$\frac{dN(t)}{dt} = -\frac{M_0}{\overline{M}(t)^2}\frac{d\overline{M}(t)}{dt}. \tag{S13}$$

Substituting Eq. (S13) into Eq. (S10) leads to

$$\frac{d\overline{M}(t)}{dt} = \frac{\overline{M}(t)^2}{2\,M_0\,V_0}\int_0^\infty\int_0^\infty K(M,M')P(M,t)P(M',t)\,dM'\,dM. \tag{S14}$$

Diffusion-limited cluster aggregation

The physical processes governing the rate of cluster coagulation vary depending on the specific scenario. We first focus on diffusion-limited aggregation, where cluster diffusion governs the coagulation rate. Other factors such as cluster shape and collision cross-section can also be incorporated. For a sphere of radius R surrounded by Brownian particles with diffusion constant D, the absorption rate scales as $K \sim DR^{d-2}$ [S18]. Using this, we construct the coagulation kernel for clusters:

$$K(M,M') = A\,[D(M)+D(M')]\,[R(M)+R(M')]^{d-2} = A\,(M^\alpha + M'^\alpha)\left(M^{1/d_f} + M'^{1/d_f}\right)^{d-2}, \tag{S15}$$

where A is a constant that ensures correct dimensionality (volume/time), $R \sim M^{1/d_f}$ is the radius of gyration with fractal dimension d_f, and $D(M) \sim M^\alpha$ is the diffusion-mass scaling (observed in our simulations here and in other references such as Ref. [S22]). Unlike fixed spheres absorbing particles, here clusters themselves diffuse and merge, thus the kernel includes sums of diffusion constants and radii.

Substituting Eq. (S15) into Eq. (S14), we get

$$\frac{d\overline{M}(t)}{dt} = \frac{A\,\overline{M}(t)^2}{2\,M_0\,V_0}\int_0^\infty\int_0^\infty (M^\alpha + M'^\alpha)\left(M^{1/d_f} + M'^{1/d_f}\right)^{d-2} P(M,t)P(M',t)\,dM'\,dM. \tag{S16}$$

From our simulations, as discussed above, we observe the dynamical scaling form [S17]

$$P(M,t) = \overline{M}(t)^{-2} f\left(\frac{M}{\overline{M}(t)}\right). \tag{S17}$$

Applying the change of variables $x = M/\overline{M}(t)$ and $x' = M'/\overline{M}(t)$, Eq. (S16) becomes

$$\begin{aligned}\frac{d\overline{M}(t)}{dt} &= \frac{A\overline{M}(t)^{\alpha+\frac{d-2}{d_f}}}{2M_0V_0}\int_0^\infty\int_0^\infty (x^\alpha + x'^\alpha)(x^{1/d_f} + x'^{1/d_f})^{d-2} f(x)f(x')\,dx\,dx' \\ &= C_1\overline{M}(t)^{\alpha+\frac{d-2}{d_f}}, \end{aligned} \tag{S18}$$

where

$$I_1 = \int_0^\infty\int_0^\infty (x^\alpha + x'^\alpha)(x^{1/d_f} + x'^{1/d_f})^{d-2} f(x)f(x')\,dx\,dx' \tag{S19}$$

is a constant, and

$$C_1 = \frac{AI_1}{2M_0V_0}. \tag{S20}$$

Integrating Eq. (S18) with initial condition $\overline{M}(0) = 1$ yields

$$\overline{M}(t) = \left[C_1\left(1-\alpha-\frac{d-2}{d_f}\right)t+1\right]^{\frac{d_f}{d_f-d_f\alpha-(d-2)}} \sim t^z, \tag{S21}$$

with the dynamic exponent

$$z = \frac{d_f}{d_f - d_f\alpha - (d-2)}. \tag{S22}$$

In two dimensions ($d = 2$), this simplifies to

$$z = \frac{1}{1-\alpha}. \tag{S23}$$

Hence, the average cluster mass grows algebraically in time as a direct consequence of the dynamical scaling hypothesis.

Ballistic aggregation

In ballistic aggregation, cluster collisions are dominated by their relative velocity. A commonly used kernel in the literature is [S16, S17]

$$K(M,M') = B\,|V(M) - V(M')|\,(R(M) + R(M'))^{d-1} = B\,|M^\gamma - M'^\gamma|\left(M^{1/d_f} + M'^{1/d_f}\right)^{d-1}. \tag{S24}$$

Here, $|V(M) - V(M')|$ originates from the relative velocity between clusters and the term $(R(M) + R(M'))^{d-1}$ corresponds to their collision cross-section. As we observed in our simulations, the typical cluster speed scales with mass as $V \sim M^\gamma$. For clusters composed of particles with uncorrelated self-propulsions, $\gamma = -1/2$, whereas for fully aligned clusters, $\gamma = 0$.

Substituting Eq. (S24) into Eq. (S14) yields

$$\frac{d\overline{M}(t)}{dt} = \frac{B\overline{M}(t)^2}{2M_0V_0}\int_0^\infty\int_0^\infty |M^\gamma - M'^\gamma|\left(M^{1/d_f} + M'^{1/d_f}\right)^{d-1} P(M,t)P(M',t)\,dM'\,dM. \tag{S25}$$

Applying the scaling ansatz Eq. (S17), and changing variables as before, leads to

$$\begin{aligned}\frac{d\overline{M}(t)}{dt} &= \frac{B\overline{M}(t)^{\gamma+\frac{d-1}{d_f}}}{2M_0V_0}\int_0^\infty\int_0^\infty |x^\gamma - x'^\gamma|(x^{1/d_f} + x'^{1/d_f})^{d-1} f(x)f(x')\,dx\,dx' \\ &= C_2\overline{M}(t)^{\gamma+\frac{d-1}{d_f}}, \end{aligned} \tag{S26}$$

where

$$I_2 = \int_0^\infty \int_0^\infty |x^\gamma - x'^\gamma|(x^{1/d_f} + x'^{1/d_f})^{d-1} f(x) f(x')\, dx\, dx' \tag{S27}$$

is a constant and

$$C_2 = \frac{BI_2}{2M_0V_0}. \tag{S28}$$

Integrating Eq. (S26) with $\overline{M}(0) = 1$ gives

$$\overline{M}(t) = \left[C_2 \left(1 - \gamma - \frac{d-1}{d_f}\right) t + 1\right]^{\frac{d_f}{d_f - d_f\gamma - (d-1)}} \sim t^z, \tag{S29}$$

where the dynamic exponent is

$$z = \frac{d_f}{d_f - d_f\gamma - (d-1)}. \tag{S30}$$

In the limit of compact, non-fractal clusters where the spatial dimension equals the fractal dimension, $d = d_f$, the dynamic exponent reduces to

$$z = \frac{d}{1 - d\gamma}. \tag{S31}$$

Again, the average cluster mass grows algebraically in time with the exponent z depending on the scaling of speed, fractal dimension, and system dimension. For $d = 2$, we obtain $z = \frac{2}{1-2\gamma}$ as discussed in the main text. In particular, for non-collective ballistic aggregation, one has $\gamma = -1/2$ and we obtain $z = 1$.

—

Conclusions

In this chapter, we summarize the main findings of the two research lines developed in this thesis and outline possible perspectives for their continuation.

4.1 Differential Contractility and Segregation

In the first part, we addressed the long-standing *Differential Surface Contraction Hypothesis* (DSCH) proposed by Harris, which posits that cell segregation can be driven by differences in active cortical contractility rather than adhesion. To test this hypothesis in isolation, we developed a computational model of *deformable active membranes*, where each cell is represented as an active elastic ring with tunable contractility at cell–cell interfaces. This approach allowed us to independently control DSCH-related parameters and exclude confounding effects of adhesion. Through large-scale simulations, we found that segregation emerges when the contractility ratio between cell types exceeds a threshold ($\Lambda > 1$), while for $\Lambda < 1$ the system develops a chessboard-like arrangement. The coarsening process exhibited algebraic growth of the average cluster mass, $\overline{M}(t) \sim t^z$, with $z \approx 2/3$. Although this exponent matches the Lifshitz–Slyozov–Wagner prediction for Ostwald ripening, our analysis of microstructural dynamics revealed that domain growth was dominated by *coalescence of entire clusters* rather than evaporation-condensation.

Perspectives: *Interaction between Contractility and Adhesion:* A natural extension of the present work is to incorporate *differential adhesion* into the model [44]. This would enable the study of possible synergies or competitions between the DAH (Differential Adhesion Hypothesis) and the DSCH (Differential Surface Contractility Hypothesis). How does the segregation threshold ($\Lambda = 1$) shift in the presence of differential adhesion? Is there a regime where one mechanism dominates over the other? Addressing these questions would directly tackle the problem of how different forces combine to generate the effective interfacial tension in tissues.

Activity as contractile tension fluctuations: An alternative perspective is to redefine cellular activity. Instead of originating from self-propulsion, activity can be modeled as stochastic fluctuations in the contractile tensions themselves, driven by subcellular dynamics such as myosin motor turnover [54, 74]. This framework allows testing whether such fluctuations alone can fluidize the tissue and drive segregation. Furthermore, it opens the door to exploring a novel, kinetically-driven sorting mechanism based on *differential fluctuations*, where heterotypic junctions have a higher fluctuation magnitude ($\sigma_{\neq}$) than homotypic ones ($\sigma_{=}$).

Non-reciprocal Interactions and Friction: In living systems, interactions are not necessarily reciprocal, the force exerted by cell A on cell B may differ from that exerted by B on A. The model could be extended to explore the case where $\Lambda_{12} \neq \Lambda_{21}$ [75–77]. Such a breaking of Newton's third law is a hallmark of active systems and can give rise to entirely

new mechanical phenomena, such as *odd elasticity*. Furthermore, investigating the role of *friction* and *dissipation* at the cell–cell interface could reveal novel types of instabilities or pattern formation [67, 78].

4.2 Aggregation Kinetics in Active Matter

In the second part, we investigated *cluster aggregation kinetics* in active matter systems, aiming to connect microscopic motion rules to macroscopic domain growth laws. We formulated the problem within the *Smoluchowski coagulation equation* framework, identifying the coagulation kernel as the key link between particle-level dynamics and scaling exponents. Two limiting regimes were considered: *Diffusion-Limited Cluster Aggregation* (DLCA), with z ranging from 1/2 to 1 depending on velocity correlations, and *ballistic aggregation*, with z ranging from 1 to ≥ 2. This classification captures the scaling behavior of a broad range of passive and weakly active systems. However, experimental studies on cellular systems (e.g., Méhes *et al.* [**?**]) reported exponents up to $z \approx 1.5$, inconsistent with purely diffusive or classical ballistic motion.

To address this, we developed a model of *adhesive self-propelled particles with internal alignment*, showing that a *flocking transition at the cluster level* can drastically increase the persistence length of cluster trajectories. When the persistence length grows faster with cluster mass than the average inter-cluster separation, the system enters a *collective ballistic aggregation regime*, where $z \simeq 2$ (and even higher if clusters are fractal). This mechanism unifies diffusive, ballistic, and collective ballistic coarsening within the same theoretical framework and reconciles experimental high-z values with first-principles modeling.

Perspectives: Future work should aim to enhance the model's realism and expand its scope. To assess the degree of realism of our framework, key model parameters could be determined experimentally. The model could also be refined by incorporating additional properties of the surrounding medium, such as viscoelasticity [3] and contact inhibition [72], which are known to modulate aggregation kinetics. An important next step is to extend the model to include *fragmentation processes*, enabling a more complete description of aggregation–disaggregation dynamics and steady-state cluster size distributions [79]. Another promising direction is to perform simulations with *binary mixtures* featuring *non-reciprocal interactions* in terms of adhesion and alignment, to explore how such asymmetries affect the kinetics of aggregation and the resulting scaling laws [75, 76].

This thesis has theoretically and numerically explored the physical principles underlying cell segregation and aggregation in active matter, using minimal yet physically grounded models that bridge mechanical hypotheses and kinetic theory. By isolating DSCH and uncovering the role of *cluster-level collective motion* in driving anomalously fast coarsening, the work advances our mechanistic understanding of tissue patterning and provides a unified framework for interpreting experimental scaling laws in living and synthetic active systems. From deformable active membranes to flocking-driven cluster aggregation, the results highlight the richness of active matter dynamics and open new avenues for linking microscopic activity rules to emergent macroscopic organization.

Bibliography

[1] M. S. Steinberg, Science **141**, 401 (1963).

[2] J. P. Rieu, N. Kataoka, and Y. Sawada, Phys. Rev. E **57**, 924 (1998).

[3] D. A. Beysens, G. Forgacs, and J. A. Glazier, Proceedings of the National Academy of Sciences **97**, 9467 (2000).

[4] M. Krieg, Y. Arboleda-Estudillo, P.-H. Puech, J. Käfer, F. Graner, D. Müller, and C.-P. Heisenberg, Nature cell biology **10**, 429 (2008).

[5] E. Méhes, E. Mones, V. Nemeth, and T. Vicsek, PloS one **7**, e31711 (2012).

[6] O. Cochet-Escartin, T. T. Locke, W. H. Shi, R. E. Steele, and E.-M. S. Collins, Biophysical Journal **113**, 2827 (2017).

[7] E. Méhes, E. Mones, M. Varga, Á. Zsigmond, B. Biri-Kovács, L. Nyitray, V. Barone, G. Krens, C.-P. Heisenberg, and T. Vicsek, Communications biology **6**, 817 (2023).

[8] T. Vicsek, A. Czirók, E. Ben-Jacob, I. Cohen, and O. Shochet, Phys. Rev. Lett. **75**, 1226 (1995).

[9] C. A. La Porta, S. Zapperi, et al., Cell migrations: Causes and functions, Vol. 1146 (Springer, 2019).

[10] T. Vicsek and A. Zafeiris, Physics Reports **517**, 71 (2012).

[11] A. Manacorda, Lattice Models for Fluctuating Hydrodynamics in Granular and Active Matter (Springer, 2018).

[12] S. R. K. Vedula, M. C. Leong, T. L. Lai, P. Hersen, A. J. Kabla, C. T. Lim, and B. Ladoux, Proceedings of the National Academy of Sciences **109**, 12974 (2012).

[13] D. Bi, X. Yang, M. C. Marchetti, and M. L. Manning, Phys. Rev. X **6**, 021011 (2016).

[14] A. K. Harris, Journal of theoretical biology **61**, 267 (1976).

[15] M. L. Manning, R. A. Foty, M. S. Steinberg, and E.-M. Schoetz, Proc Natl Acad Sci U S A **107**, 12517 (2010).

[16] G. Salbreux, G. Charras, and E. Paluch, Trends in cell biology **22**, 536 (2012).

[17] N. C. Heer and A. C. Martin, Development **144**, 4249 (2017).

[18] L. Canty, E. Zarour, L. Kashkooli, P. François, and F. Fagotto, Nature communications **8**, 157 (2017).

[19] B. Szabo, G. Szöllösi, B. Gönci, Z. Jurányi, D. Selmeczi, and T. Vicsek, Physical Review E **74**, 061908 (2006).

[20] P. Baconnier, O. Dauchot, V. Démery, G. Düring, S. Henkes, C. Huepe, and A. Shee, Rev. Mod. Phys. **97**, 015007 (2025).

[21] G. W. Brodland, J. Biomech. Eng. **124**, 188 (2002).

[22] I. Lifshitz and V. Slyozov, Journal of Physics and Chemistry of Solids **19**, 35 (1961).

[23] C. Wagner, Zeitschrift für Elektrochemie, Berichte der Bunsengesellschaft für physikalische Chemie **65**, 581 (1961).

[24] P. W. Voorhees, Journal of Statistical Physics **38**, 231 (1985).

[25] F. Leyvraz, Physics Reports **383**, 95 (2003).

[26] A. Moncho-Jordá, G. Odriozola, M. Tirado-Miranda, A. Schmitt, and R. Hidalgo-Álvarez, Phys. Rev. E **68**, 011404 (2003).

[27] E. Matijevic and R. J. Good, Surface and colloid science, Vol. 12 (Springer Science & Business Media, 2012).

[28] P. L. Krapivsky, S. Redner, and E. Ben-Naim, A kinetic view of statistical physics (Cambridge University Press, 2010).

[29] Y. Jiang and F. Leyvraz, Journal of Physics A: Mathematical and General **26**, L179 (1993).

[30] E. Mones, A. Czirók, and T. Vicsek, New journal of physics **17**, 063013 (2015).

[31] C. P. Beatrici, R. M. de Almeida, and L. G. Brunnet, Physical Review E **95**, 032402 (2017).

[32] H. H. Chen, Finite element-based computer simulation of motility, sorting, and deformation in l (University of Waterloo, 1998).

[33] R. G. Harrison, Journal of Experimental Zoology **9**, 787 (1910).

[34] A. Moscona, Experimental Cell Research **3**, 535 (1952).

[35] J. P. Trinkaus and P. W. Groves, Proceedings of the National Academy of Sciences **41**, 787 (1955).

[36] P. Weiss and R. James, Exptl. Cell Research (1955).

[37] P. Weiss and A. Taylor, Proceedings of the National Academy of Sciences **46**, 1177 (1960).

[38] H. B. Wolff, L. A. Davidson, and R. M. Merks, Bulletin of Mathematical Biology **81**, 3322 (2019).

[39] F. Graner, Journal of Theoretical Biology **164**, 455 (1993).

[40] F. Graner and Y. Sawada, Journal of Theoretical Biology **164**, 477 (1993).

[41] F. m. c. Graner and J. A. Glazier, Phys. Rev. Lett. **69**, 2013 (1992).

[42] J. A. Glazier and F. m. c. Graner, Phys. Rev. E **47**, 2128 (1993).

[43] M. Durand, PLOS Computational Biology **17**, e1008576 (2021).

[44] J. M. Belmonte, G. L. Thomas, L. G. Brunnet, R. M. C. de Almeida, and H. Chaté, Phys. Rev. Lett. **100**, 248702 (2008).

[45] G. Grégoire and H. Chaté, Phys. Rev. Lett. **92**, 025702 (2004).

[46] G. S. Redner, A. Baskaran, and M. F. Hagan, Physical Review E—Statistical, Nonlinear, and Soft Matter Physics **88**, 012305 (2013).

[47] J. M. Osborne, A. G. Fletcher, J. M. Pitt-Francis, P. K. Maini, and D. J. Gavaghan, PLoS computational biology **13**, e1005387 (2017).

[48] D. Sarkar, G. Gompper, and J. Elgeti, Communications Physics **4**, 1 (2021).

[49] J. D. Amack and M. L. Manning, Science **338**, 212 (2012).

[50] G. W. Brodland, in Seminars in cell & developmental biology, Vol. 47 (Elsevier, 2015) pp. 62–73.

[51] G. W. Brodland and H. H. Chen, Journal of Biomechanics **33**, 845 (2000).

[52] G. W. Brodland, Appl. Mech. Rev. **57**, 47 (2004).

[53] S. Gsell, S. Tlili, M. Merkel, and P.-F. Lenne, Nature Physics , 1 (2025).

[54] M. Krajnc, Soft Matter **16**, 3209 (2020).

[55] D. L. Barton, S. Henkes, C. J. Weijer, and R. Sknepnek, PLoS computational biology **13**, e1005569 (2017).

[56] P. Sahu, D. M. Sussman, M. Rübsam, A. F. Mertz, V. Horsley, E. R. Dufresne, C. M. Niessen, M. C. Marchetti, M. L. Manning, and J. M. Schwarz, Soft Matter **16**, 3325 (2020).

[57] B.-q. Ai and R.-x. Guo, Physical Review E **104**, 064411 (2021).

[58] D. Bi, J. Lopez, J. M. Schwarz, and M. L. Manning, Nature Physics **11**, 1074 (2015).

[59] S. Arzash, I. Tah, A. J. Liu, and M. L. Manning, Phys. Rev. Res. **7**, 013157 (2025).

[60] O. K. Damavandi, S. Arzash, E. Lawson-Keister, and M. L. Manning, PRX Life **3**, 033001 (2025).

[61] M. Skamrahl, J. Schünemann, M. Mukenhirn, H. Pang, J. Gottwald, M. Jipp, M. Ferle, A. Rübeling, T. A. Oswald, A. Honigmann, et al., Proceedings of the National Academy of Sciences **120**, e2213186120 (2023).

[62] A. K. O'Neill, A. A. Kindberg, T. K. Niethamer, A. R. Larson, H.-Y. H. Ho, M. E. Greenberg, and J. O. Bush, Journal of Cell Biology **215**, 217 (2016).

[63] A. A. Kindberg, V. Srivastava, J. M. Muncie, V. M. Weaver, Z. J. Gartner, and J. O. Bush, Journal of Cell Biology **220**, e202005216 (2021).

[64] E. F. Teixeira, C. P. Beatrici, H. C. M. Fernandes, and L. G. Brunnet, Phys. Rev. Lett. **134**, 138401 (2025).

[65] E. F. Teixeira, H. C. Fernandes, and L. G. Brunnet, Soft Matter **17**, 5991 (2021).

[66] G. Ourique, E. Teixeira, and L. Brunnet, Physica A: Statistical Mechanics and its Applications **589**, 126661 (2022).

[67] A. Boromand, A. Signoriello, F. Ye, C. S. O'Hern, and M. D. Shattuck, Physical Review Letters **121**, 248003 (2018).

[68] J. D. Treado, D. Wang, A. Boromand, M. P. Murrell, M. D. Shattuck, and C. S. O'Hern, Physical Review Materials **5**, 055605 (2021).

[69] M. v. Smoluchowski, Z. Physik. **17**, 585 (1916).

[70] D. J. Aldous, Bernoulli **5**, 3 (1999).

[71] P. Cremer and H. Löwen, Phys. Rev. E **89**, 022307 (2014).

[72] M. Bothe, E. Lardet, A. Poliakov, G. Pruessner, T. Bertrand, and I. Bordeu, arXiv preprint arXiv:2503.13714 (2025).

[73] N. Shimoyama, K. Sugawara, T. Mizuguchi, Y. Hayakawa, and M. Sano, Phys. Rev. Lett. **76**, 3870 (1996).

[74] Y.-E. Keta and S. Henkes, Soft Matter (2025).

[75] K. L. Kreienkamp and S. H. L. Klapp, Phys. Rev. Lett. **133**, 258303 (2024).

[76] K. L. Kreienkamp and S. H. Klapp, Physical Review E **110**, 064135 (2024).

[77] B. Sahoo, R. Mandal, and P. Sollich, arXiv preprint arXiv:2508.02814 (2025).

[78] M. L. Manning, Phys. Rev. Lett. **130**, 130002 (2023).

[79] F. Peruani, J. Starruß, V. Jakovljevic, L. Søgaard-Andersen, A. Deutsch, and M. Bär, Physical review letters **108**, 098102 (2012).